

1 **Spectral induced polarization characterization of**
2 **non-consolidated clays for varying salinities - an**
3 **experimental study**

4 **Aida Mendieta¹, Damien Jougnot¹, Philippe Leroy², and Alexis Maineult¹**

5 ¹Sorbonne Université, CNRS, EPHE, UMR 7619 METIS, 75005 Paris, France

6 ²BRGM, French Geological Survey, 45060 Orléans, France

7 **Key Points:**

- 8 • The quadrature conductivity of clays behaves non-monotonously with increasing
9 salinity
- 10 • Some polarization mechanisms may cease to act or decrease significantly at a spe-
11 cific salinity
- 12 • The quadrature to surface conductivity ratio is lower for clays than for other min-
13 erals

Corresponding author: Aida Mendieta, aida.mendieta_tenorio@upmc.fr

14 Abstract

15 Clay material characterization is of importance for many geo-engineering and environ-
 16 mental applications, and geo-electrical methods are often used to detect them in the sub-
 17 surface. Spectral induced polarization (SIP) is a geo-electric method that non-intrusively
 18 measures the frequency-dependent complex electrical conductivity of a material, in the
 19 mHz to the kHz range. We present a new SIP dataset of four different types of clay (a
 20 red montmorillonite sample, a green montmorillonite sample, a kaolinite sample, and an
 21 illite sample) at five different salinities (initially de-ionized water, 10^{-3} , 10^{-2} , 10^{-1} , and
 22 1 mol/L of NaCl). We propose a new laboratory protocol that allows the repeatable char-
 23 acterization of clay samples. The complex conductivity spectra are interpreted with the
 24 widely used phenomenological double-Pelton model. We observe an increase of the real
 25 part of the conductivity with salinity for all types of clay, while the imaginary part presents
 26 a non monotonous behavior. The decrease of imaginary conductivity (sensitive to po-
 27 larization mechanisms) over real conductivity with salinity is interpreted as evidence that
 28 conduction due to electromigration processes increases with salinity faster than conduc-
 29 tion due to polarization processes. We test the empirical petrophysical relationship be-
 30 tween σ''_{surf} and σ'_{surf} and validate this approach based on our experimental data and
 31 two other datasets from the literature. With this dataset we can better understand the
 32 frequency-dependent electrical response of different types of clay. This unique dataset
 33 of complex conductivity spectra for different types of clay samples is a step forward to-
 34 ward better characterization of clay formations in situ.

35 1 Introduction

36 Clay minerals are ubiquitous in the Earth's subsurface and can be found in many
 37 geological formations, from hard clay rocks to disseminated clay aggregates or lenses in
 38 other sedimentary rocks. These minerals are frequently the main components of extended
 39 sedimentary stratigraphic layers. Illite and smectite alone may constitute around 30%
 40 of all sedimentary rocks (Garrels & Mackenzie, 1971). Clay materials are fine-grained
 41 soil materials (particle size below 2 μm) characterized by a large fraction of nanopores,
 42 high specific surface area (between 10 and 1000 m^2/g), and a large negative surface charge
 43 (between -0.15 and -0.10 Cm^{-2}) (e.g., Michot & Villieras, 2006), thus large cationic ex-
 44 change capacity (CEC, between 0.03 and 1.5 meq g^{-1}) and low permeability (typically
 45 below 10^{-16}m^2) (Revil & Leroy, 2004). These properties make clay formations suitable

46 to be, e.g.: cap rocks forming geo-reservoirs, aquitards defining the geometry of hydrosys-
47 tems, or potential hosts for waste repositories. Studying the transport and mechanical
48 properties of clay materials is crucial for many geoenvironmental and environmental appli-
49 cations, such as: oil and gas (e.g., Morsy & Sheng, 2014), geothermal energy exploration
50 and production (e.g., Corrado et al., 2014), critical zone research (e.g., Chorover et al.,
51 2007), nuclear waste storage (e.g., Gonçalves et al., 2012; Ortiz et al., 2002), hydroge-
52 ology (e.g., Parker et al., 2008; Konikow et al., 2001), civil engineering (e.g., Islam et al.,
53 2020), among others.

54 Clay formations are geological formations composed of a majority of clay minerals. Clay
55 minerals are hydrous aluminium phyllosilicates, that is, silicates organized in stacks of
56 tetrahedral (T) silica sheets and aluminium octahedral (O) sheets called platelets (Bergaya
57 & Lagaly, 2006). The T and O sheets present an overall negative electrical charge at their
58 surfaces because of deprotonated oxygen atoms and isomorphous substitutions in the crys-
59 tal lattice (Leroy & Revil, 2004). Due to these charges on the clay surface, cations (e.g.:
60 Ca^{2+} , Na^+ , Mg^{2+} , K^+) can be adsorbed in the interlayer space of illite, smectite and
61 chlorite minerals between platelets; and on the external surface in the electrical double
62 layer (EDL) made of the Stern and diffuse layer (Leroy & Revil, 2009). The differences
63 between clay minerals depend on the kind of tetrahedral and octahedral stacks (1:1 for
64 TO or 2:1 for TOT) and adsorbed cations in the interlayer space (e.g., K^+ for illite or
65 Na^+ and Ca^{2+} for montmorillonite) (Brigatti et al., 2006). The clay platelets are then
66 organized in tactoids, that is, stacks of platelets having different geometries, which form
67 aggregates (Bergaya & Lagaly, 2006). There are four main groups of clay minerals: kaoli-
68 nite, illite, smectite, and chlorite.

69 The total specific surface area of a kaolinite tactoid, typically 10-20 m^2/g , is consider-
70 ably lower than the total specific surface area of an illite and montmorillonite tactoid
71 (typically 100-200 m^2/g for illite and 750-800 m^2/g for Na-montmorillonite)(Hassan et
72 al., 2006; Revil & Leroy, 2004; Tournassat et al., 2011, 2015). Clay formations can be
73 constituted of a mixture or stratifications of different clay minerals (e.g., inter-stratified
74 illite-smectite). In the present work, we focus on the three more common groups: kaoli-
75 nite (1:1), illite (2:1), and smectite (2:1, montmorillonites are part of the smectite fam-
76 ily). As presented previously, kaolinite, illite and smectite groups present many differ-
77 ent characteristics in terms of structure (e.g., number of stacked platelets, tactoid size
78 and shape), physicochemical properties (e.g., surface charges, CEC), mechanical prop-

79 erties (e.g., plasticity, resistance to stress, swelling-shrinking), and also electrical prop-
80 erties. It is therefore crucial to electrically discriminate these minerals between each other
81 in order to characterize the properties of the formation or predict its behavior if submit-
82 ted to stress (e.g., hydraulic, mechanic, thermic).

83 In geophysics, the most common methods to identify the presence of clay minerals non-
84 intrusively in the field are electrical and electromagnetic methods (e.g., Auken et al., 2017):
85 direct current electrical resistivity tomography (ERT) (e.g., Batayneh, 2006), induced
86 polarization (IP) (e.g., Okay et al., 2013; Lévy et al., 2019a), time-domain electromag-
87 netics (TDEM) (e.g., Finco et al., 2018), frequency-domain (FDEM) electromagnetics
88 (e.g., Spichak & Manzella, 2009), and ground penetrating radar (GPR) (e.g., Looms et
89 al., 2018). However, if clays are usually associated to high electrical conductivity zones,
90 they can be mistaken with highly mineralized pore water when only the real electrical
91 conductivity is considered. One way to avoid this misinterpretation is to use the com-
92 plex conductivity (inferred from IP), that is the real and imaginary parts of the conduc-
93 tivity, or its spectral behavior, i.e. the dependence with frequency of the conductivity,
94 to extract more information than from a single frequency measurement.

95 The spectral induced polarization (SIP) method can investigate the conduction and po-
96 larization of geological materials over a large range of frequencies: from the mHz to the
97 kHz (e.g., Kemna et al., 2012; Revil et al., 2012). Indeed, in addition to the resistivity,
98 the SIP method gives the chargeability of the investigated porous medium, which describes
99 its capability to reversibly store electrical charges (Revil et al., 2012). The chargeabil-
100 ity is very sensitive to the pore structure and electrical surface properties (Leroy & Re-
101 vil, 2009). When SIP measurements are coupled with a relevant petrophysical model,
102 they can provide information on the nature and behavior of electrical phenomena (con-
103 duction and polarization) happening at the pore scale (Revil, 2012), helping to interpret
104 field scale geophysical electrical measurements in terms of mineralogy, pore structure,
105 water content, and permeability distribution (Okay et al., 2013; Ghorbani et al., 2009).

106 The frequency-dependent electrical response of clay minerals has been recently studied
107 in well-controlled conditions in the laboratory. Many clayey materials have been stud-
108 ied, from mixtures containing sand and clays (e.g., Breede et al., 2012; Okay et al., 2014;
109 Wang & Slater, 2019), synthetic clay suspensions (e.g., Leroy et al., 2017), to natural clays
110 and clayrocks (e.g., Lévy et al., 2018; Jougnot et al., 2010). These measurements have

111 been performed in saturated (e.g., Lévy et al., 2019b) or partially water-saturated (e.g.,
112 Cosenza et al., 2008; Ghorbani et al., 2009; Jougnot et al., 2010) conditions.

113 However, as pointed out by Leroy & Revil (2009) and Leroy et al. (2017), there is a lack
114 of SIP laboratory studies on individual clay minerals. Indeed, measuring the frequency-
115 dependent electrical response of individual clay minerals is of great importance to bet-
116 ter understand their specific conduction and polarization and to improve their geophys-
117 ical imaging. This is needed in order to move towards a full discrimination of clay min-
118 erals when interpreting field electrical measurements. This can only be achieved by bet-
119 ter understanding the electrical signal of each individual type of clay. In this paper, we
120 intend to characterize the electrical signal of a variety of clay samples at multiple fre-
121 quencies (from mHz to kHz) and at multiple salinities (from initially de-ionized water
122 to 1 mol/L of NaCl) using laboratory SIP measurements on three groups of clay min-
123 erals: illite, smectite, and kaolinite.

124 In the present contribution, we first present the method and some theoretical background
125 for the SIP of clay materials. Then, we detail the protocol we propose in order to ob-
126 tain the clay samples, characterize them, perform the SIP measurements, and post-treat
127 them. We present the results on four clay samples (two smectite samples, a kaolinite sam-
128 ple, and an illite sample) at five different salinities (initially de-ionized water, 10^{-3} , 10^{-2} , 10^{-1} ,
129 and 1 mol/L of NaCl) and analyze them using a phenomenological model. Finally, we
130 discuss our results with respect to the existing literature.

131 **2 Theory**

132 **2.1 Characteristics of kaolinite, illite, and montmorillonite**

133 As mentioned earlier, clay minerals have a strong electrical conductivity response
134 due to the high surface conductivity associated with the high electrical charge on their
135 surface (Revil & Leroy, 2004; Revil, 2012). This particularity, in addition to the hetero-
136 geneities of the surface electrical properties of clay minerals (Leroy & Revil, 2004), makes
137 clay systems quite complex but also, interesting to characterize electrically.

138 Kaolinite is a 1:1 clay, composed of a succession of silica tetrahedral (T) and aluminum
139 octahedral (O) sheets (see Figure 1a) whereas illite and montmorillonite (member of the
140 smectite group) are 2:1 clays made up of a succession of TOT sheets (see Figure 1b) (Leroy
141 & Revil, 2009). The thickness of a TOT platelet is around 9.5 \AA , its length is around

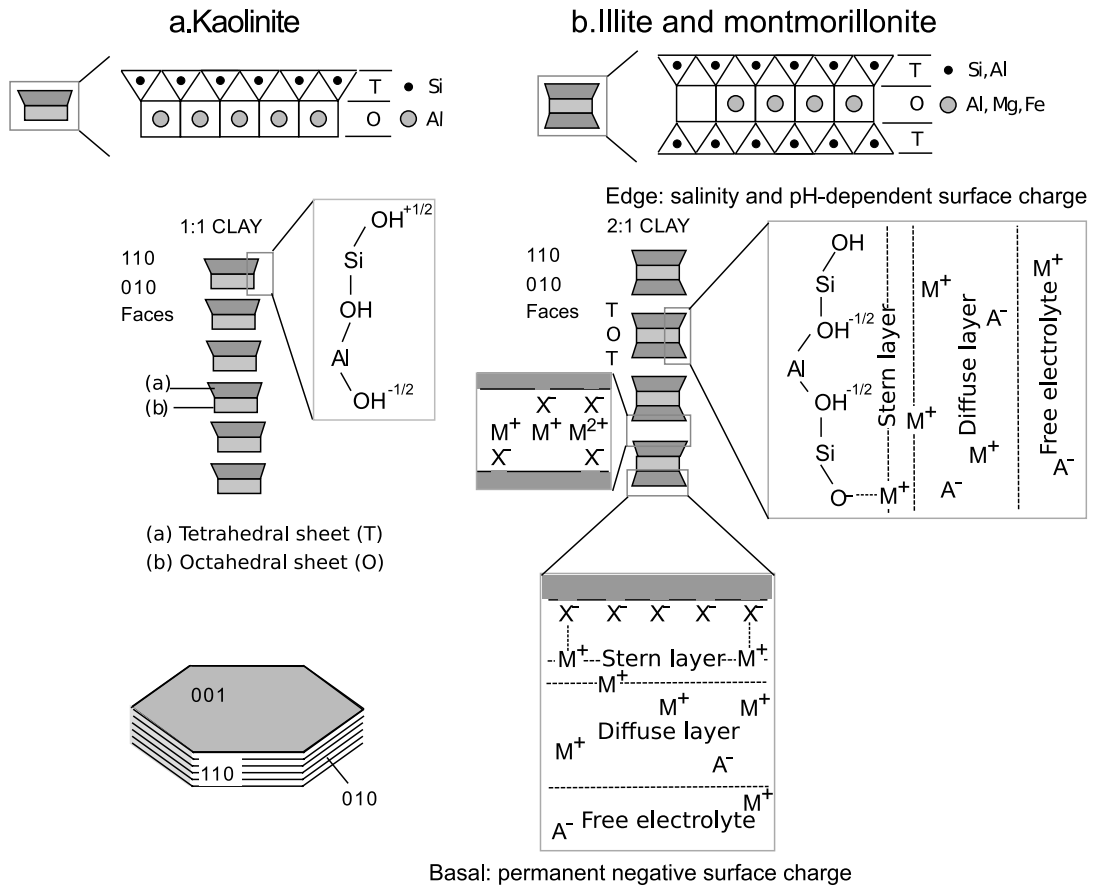


Figure 1. Sketch of a (a) kaolinite and an (b) illite or montmorillonite clay tactoid showing the different types of surface sites on the basal and edge surfaces as well as the electrical double layer around them (electrical double layer not shown for kaolinite) and the interlayer space between TOT sheets (modified from Leroy & Revil, 2009).

142 50-100 nm for illite and 50-1000 nm for montmorillonite (Tournassat et al., 2015). For
143 kaolinite, the thickness of a TO platelet is around 7 Å and its length lies between around
144 200 nm to more than 1000 nm (Tournassat & Steefel, 2015). The number of stacked lay-
145 ers of a kaolinite tactoid ranges from 10 to more than 200 whereas this number ranges
146 between 1 and 2, 6 and 10, and 5 and 20 for Na-montmorillonite, Ca-montmorillonite
147 and illite, respectively (Tournassat et al., 2015; Tournassat & Steefel, 2015; Leroy et al.,
148 2017). The height of a kaolinite tactoid ranges between 7 and 150 nm and the height of
149 an illite and montmorillonite tactoid lies between 5 and 20 nm, and, 1 and 10 nm, re-
150 spectively (Hassan et al., 2006; Tournassat et al., 2011; Tournassat & Steefel, 2019). It
151 results that the total specific surface area of a kaolinite tactoid is considerably lower than
152 the total specific surface area of an illite and montmorillonite tactoid (typically, 10-20
153 m²/g versus 100-200 m²/g and 750-800 m²/g, respectively).

154 Consequently, clay minerals generally present a high aspect ratio with different morpholo-
155 gies: kaolinite and well-crystallized illite have a tendency toward hexagonal and elongated
156 hexagonal morphologies respectively, whereas montmorillonite and less well-crystallized
157 illite have mostly irregular platy or lath-shaped morphologies. The surface charge of the
158 lateral surface of kaolinite, illite and montmorillonite (to a lesser extent due to the in-
159 fluence of the basal surface) are controlled by the aluminol and silanol (>Al-OH and >Si-
160 OH) surface sites and are thus sensitive to salinity and pH (Tombácz & Szekeres, 2006).
161 When salinity and pH increase, the charge on these surfaces is generally more negative
162 due to the >Si-O- surface sites. On the other hand, the basal surface of illite and mon-
163 torillonite is permanently negative and less sensitive to salinity and pH because it mainly
164 results from the isomorphic substitutions in the crystal lattice (e.g., Si⁴⁺ by Fe³⁺ or Al³⁺
165 ions in the T-sheet or Al³⁺ by Mg²⁺ or Fe²⁺ ions in the O-sheet). Most of the isomor-
166 phic substitutions in these minerals occur in the O-sheet. Because the specific surface
167 area of the basal surface of these 2:1 clays is more than one order of magnitude higher
168 than the specific surface area of the lateral surface (typically 760 m²/g vs 20 m²/g) (Tour-
169 nassat et al., 2011), the basal surface may control the surface electrical properties of il-
170 lite and montmorillonite. The CEC method can be used to measure the surface prop-
171 erties and then the surface charge of illite and montmorillonite, if the specific surface area
172 is known (Okay et al., 2014). For kaolinite, the CEC is very sensitive to pH and salin-
173 ity due to the pH and salinity dependent surface charge of the lateral surface. When a
174 clay particle is put in water, an EDL mostly made of counterions builds up to compen-

175 sate the external negative surface charge (Leroy et al., 2015; Tsujimoto et al., 2013). The
176 internal negative surface charge of montmorillonite is compensated by cations in the in-
177 terlayer space. The pore space is then made of the EDL and the free electrolyte. The
178 EDL is thought to be composed of two portions, the Stern and the diffuse layer. The Stern
179 layer is only made of counterions (cations for clays) and is thought to be fixed to the sur-
180 face of the mineral (see Figure 1). The diffuse layer is made mostly of counter-ions that
181 are more mobile than those of the Stern layer. When a clay particle and its surround-
182 ing electrolyte is submitted to a frequency dependent electrical field (for frequencies typ-
183 ically lower than 1 MHz), cations and anions around the clay particle separate, giving
184 rise to different types of polarization mechanisms.

185 In the literature, three different polarization mechanisms have been proposed for clay
186 samples in the mHz to the kHz frequency range: Maxwell-Wagner polarization, EDL po-
187 larization, and membrane polarization (e.g., Kemna et al., 2012; Chen & Or, 2006; Leroy
188 & Revil, 2009; Bücke & Hördt, 2013; Bücke et al., 2019). The Maxwell-Wagner polar-
189 ization mechanism is due to a charge build-up at boundaries between phases with dif-
190 ferent electrical properties (conductivity, permittivity) in geologic materials and happens
191 at the highest frequencies (in the kHz range) for SIP. The EDL polarization happens when
192 ions in the Stern and diffuse layers migrate around the surface of the mineral guided on
193 the orientation of the time varying external electric field, leading to a charge separation
194 in the EDL at the particle scale (Leroy et al., 2017). This polarization mechanism typ-
195 ically occurs at the mid frequencies for SIP (below the kHz range). Finally, the mem-
196 brane polarization mechanism happens when pore throats block electrical charges (an-
197 ions for clays, due to their negative electrical charge) mobilizing due to repulsive EDLs
198 and a time varying external electric field, and thus charges separate in ion selective zones.
199 This polarization mechanism happens in the lowest frequencies for SIP (typically in the
200 mHz to the Hz range). With all these polarization mechanisms the question is open on
201 what is the active polarization mechanism in clay samples at a given frequency of the
202 injected sinusoidal electrical field.

203 **2.2 Background on spectral induced polarization**

204 The SIP geophysical method consists of a sinusoidal electric current injection in
205 a rock sample and the measurement of a resulting electrical potential difference between
206 two electrodes at multiple frequencies (from mHz to kHz). In addition to the electrical

207 conductivity (or resistivity, $\rho^* = 1/\sigma^*$) of the sample, the phase-lag between injected
 208 and measured signal gives information about the petrophysical and surface electrical prop-
 209 erties of clay samples at the pore scale (e.g., Leroy et al., 2017; Kemna et al., 2012; Re-
 210 vil et al., 2012).

211 The frequency dependent complex conductivity $\sigma^*(\omega)$ is inferred from SIP. The angu-
 212 lar frequency ω (rad/s) is related to the frequency f (Hz) by $\omega = 2\pi f$. There are two
 213 ways to express the complex conductivity, either by real σ' (S m^{-1}) and imaginary com-
 214 ponents σ'' (S m^{-1}), or amplitude $|\sigma|$ (S m^{-1}) and phase φ (rad):

$$\sigma^*(\omega) = |\sigma|e^{i\varphi} = \sigma' + i\sigma'', \quad (1)$$

215 where $i = \sqrt{-1}$ represents the imaginary unit. The resulting electric signal of a rock
 216 sample depends on the electrical properties of the pore water and the rock matrix itself.
 217 Following Waxman & Smits (1968), we assume then that the measured electrical con-
 218 ductivity (a complex quantity) is a result of the bulk pore water electrical conductivity
 219 (σ_w) in the rock acting in parallel to the surface conductivity (σ_{surf}^*) of the geologic ma-
 220 terial:

$$\sigma^* = \frac{\sigma_w}{F} + \sigma_{surf}^*, \quad (2)$$

221 where F is the electrical formation factor, sensitive to the electrically connected poros-
 222 ity and the shape of the grains. For clays, surface conduction is particularly strong due
 223 to their high specific surface area and surface charge, resulting in a strong EDL (Leroy
 224 & Revil, 2004). Weller et al. (2013) took equation 2 and proposed a linear relation be-
 225 tween the real part of the measured conductivity, water conductivity, and surface con-
 226 ductivity:

$$\sigma'_{surf}(\sigma_w) = \sigma'(\sigma_w) - \frac{\sigma_w}{F}. \quad (3)$$

227 Following the notation of Weller et al. (2013), we have:

$$\sigma'' = \sigma''_{surf}. \quad (4)$$

228 Börner (1992) proposes to link the real and imaginary surface components as:

$$l = \frac{\sigma''_{surf}}{\sigma'_{surf}}. \quad (5)$$

229 2.3 Double-Pelton phenomenological model

230 In order to model SIP data there are several types of models available, some are
 231 physical models and some are phenomenological. Physical models are often complex and
 232 require a thorough knowledge of a plethora of physical and chemical properties of the
 233 rock sample in question. Phenomenological models are able to reproduce large datasets
 234 and do not require much knowledge on the physical and chemical properties of the rock
 235 sample that is being studied. We use a phenomenological double-Pelton model to fit our
 236 data. We use one Pelton model to describe the complex conductivity (the inverse of the
 237 resistivity) of the clay and the other Pelton model to explain the high frequency signal
 238 due to inductive and capacitive noise and also clay polarization. Our double-Pelton model
 239 consists of two individual Pelton (Pelton et al., 1978) electrical signals summed up to-
 240 gether. The double-Pelton model originates from the Cole-Cole and Debye models (Cole
 241 & Cole, 1941). The double-Pelton model is defined by:

$$\rho^*(\omega) = \rho_0 \left[1 - m_1 \left(1 - \frac{1}{1 + (i\omega\tau_1)^{c_1}} \right) - m_2 \left(1 - \frac{1}{1 + (i\omega\tau_2)^{c_2}} \right) \right], \quad (6)$$

242 where ρ ($\Omega \cdot m$) is the electrical resistivity of the sample (inverse of the electrical conduc-
 243 tivity σ), c (-) is the Cole-Cole exponent, τ (s) refers to the relaxation time, and m (mV/V)
 244 is the chargeability of the material. In general, ρ_0 is thought of as a direct current (DC)
 245 or low frequency term. In the case of $c=0.5$, the Pelton model becomes a Warburg model.
 246 Therefore, when in equation 6 we have $c_1 = 0.5$ and $c_2 = 0.5$, we obtain a double-Warburg
 247 model.

248 3 Materials and methods

249 3.1 CEC and XRD of clay samples

250 We performed the CEC measurements and the X-ray diffraction (XRD) charac-
 251 terization of all the clay types used in this work, to have the mineralogical composition
 252 of the samples. We present the results of the XRD analysis in Table 1. As for the CEC

Table 1. Results of XRD analysis, showing the exact content of each clay sample.

Clay sample	Smectite	Illite	Kaolinite	Gypsum	Quartz	Microcline	Albite	Calcite	Magnetite
	%	%	%	%	%	%	%	%	%
Kaolinite sample	4	3	84		10				
Illite sample		67	10			10		12	
Green mont. sample	90	1		<i>tr*</i>	1	3	1	4	
Red mont. sample	66				11	18	3		1

*tr**:traces.

253 results, we obtained: 22 meq/100 g for the kaolinite sample, 47 meq/100 g for the illite
254 sample, 132 meq/100 g for the green montmorillonite sample, and 135 meq/100 g for the
255 red montmorillonite sample. From Table 1, we see that none of our clay samples are 100%
256 pure. The XRD measurements were obtained using a Philips Xpert machine from clay
257 powder and glycolated samples. The bulk clay powder samples were quantitatively an-
258 alyzed with randomly oriented preparations following Brindley & Brown (1980) and Moore
259 & Reynolds (1989). Furthermore, following the modified Chung method (Chung, 1974;
260 Hillier, 2003) an analysis on glycolated oriented preparations was done in order to cor-
261 rect the measurements on the clay powder samples. The CEC measurement consists of
262 replacing a cation present on the clay surface with another cation (Ma & Eggleton, 1999).
263 Methods differ on the exchanged cation, the exchange solution (according to the AFNOR
264 standard NF X31-108 and Khaled & Stucki, 1991), and if there are consecutive exchanges
265 in the procedure (Ciesielski & Sterckeman, 1997; Meier & Kahr, 1999). For the CEC mea-
266 surements presented in this paper, we determined the amount of recovered Mg^{+2} ions
267 after a second exchange (Khaled & Stucki, 1991).

268 3.2 Preparation of clay samples

269 We developed a laboratory protocol that allowed us to have clay mixtures we could
270 knead and place inside a sample holder, while ensuring a good reproducibility of the data.
271 Plasticity is our criteria for a parameter to keep between all clay types, salinities and mea-
272 surements. When we talk about plasticity, we need to take a look at the Atterberg lim-
273 its in clays. The liquid and plastic limits are water contents that mark the limits of plas-
274 tic behavior of clays (White, 1949). We chose a water content within those limits for each
275 clay, to avoid a clay mixture too liquid (more water than the liquid limit), or a sample
276 too dry that crumbles into pieces (smaller water content than the plastic limit). Wag-
277 ner (2013) presents a table of liquid and plastic limits for illite, kaolinite, smectites, and
278 others. Note that Mitchell & Soga (2005) explain that the availability of ions and the
279 valence of the ions present in the pore water of the clay samples may affect these lim-
280 its. As presented in Table 2, we see a decrease of porosity at the highest salinities in our
281 clay samples, in accordance with Mitchell & Soga (2005).

282 Figure 2 describes the procedure used to prepare the clay samples. In order to obtain
283 the adequate plasticity, we first combine water and clay powder at higher water contents
284 than the objective (Figure 2a and b). We left the clay powder in contact with water for
285 at least 24 hours to have a good imbibition process, and we then mix the whole mixture
286 mechanically using a drill until we reach a homogeneous mixture (Figure 2c). In order
287 to obtain the desired water content, we eliminate the water excess through evaporation
288 by letting the clay mixture dehydrate on a polyurethane foam (Figure 2d). We use a polyurethane
289 foam to have a homogeneous evaporation process, that is, to allow evaporation from the
290 bottom, top and sides of the clay mixture. The mass of the mixture is monitored at ev-
291 ery step to determine the evolution of water content at each step of the process. After
292 obtaining the desired water content, we take the clay mixture out of the foam, knead it
293 and locate it in our sample holder (Figure 2e). Once in place, we perform the SIP mea-
294 surement of the clay sample twice, from 1 mHz to 20 kHz (see the following section and
295 Figure 2f). We acknowledge that a total chemical equilibrium might not be achieved when
296 measuring the SIP signal in the clay samples, but we assume that the difference between
297 the SIP signal we measure and a true equilibrated sample is negligible. After the mea-
298 surements are over, we take out the sample from the sample holder and dry it in an oven
299 at 105° C during 25 h (Figure 2g). By measuring the mass at every step of the process,
300 we can calculate the water content (presented in Table 2) at each step and therefore de-

301 termine the porosity of our clay sample during the SIP measurement. The calculated porosi-
 302 ties of the clay mixtures are presented in Table 2. These porosities help us keep a check
 303 on the water vs clay powder ratios of our samples. The porosity calculations present some
 304 experimental uncertainties, these porosity values are a good estimate but should not be
 305 over-interpreted.

306 Note that as the water content changed in the samples, so did the salinities. We orig-
 307 inally started all samples with five different salinities: De-ionized water (D.W.), 1×10^{-3} ,
 308 1×10^{-2} , 1×10^{-1} , and 1 M (mol/L) of NaCl. To account for the water content de-
 309 crease due to the evaporation procedure, we recalculated the salinities in our sample dur-
 310 ing the SIP measurements for all the salinities from 1×10^{-3} to 1 M of NaCl. Table 2
 311 presents the corrected salinities using a simple proportion equivalence. From these post-
 312 dehydration salinity values we calculated the bulk water electrical conductivity, follow-
 313 ing the procedure proposed in Leroy et al. (2015), using:

$$\sigma_w = e10^3 N_A \sum_{i=1}^N z_i \beta_i^w C_i^w, \quad (7)$$

314 where β_i^w (in $\text{m}^2\text{s}^{-1}\text{V}^{-1}$) is the ionic mobility of an ion i in the bulk water, C_i^w (in mol
 315 dm^{-3}) is its concentration, and z_i is its valence. Also, N_A is the Avogadro number ($6.022 \times$
 316 10^{23}mol^{-1}), and e is the elementary charge (1.602×10^{-19} C). It is worth noting that
 317 the ionic mobility values used in equation 7 have been corrected for the temperature and
 318 salinity, as presented in Leroy et al. (2015). It should be noted that the low-salinity wa-
 319 ter conductivity values may be underestimated because we do not consider clay disso-
 320 lution as well as cation leaching from the interlayer space for the calculation of the ion
 321 concentrations.

322 3.3 SIP measurement setup

323 We conducted the SIP measurements on the clay samples using the SIP-FUCHS
 324 III equipment (Radic Research, www.radic-research.de). The setup for the measurements
 325 is presented in Figure 3a. The SIP-FUCHS III sends a sinusoidal current into the sam-
 326 ple through the injection unit and then the so-called current electrodes (C1 and C2 in
 327 Figure 3b) by imposing a chosen potential difference. The second unit measures the re-
 328 sulting voltage through the so-called potential electrodes (P1 and P2 in Figure 3b). The
 329 communication between the units (injection and measurement) and the system is done

Table 2. Post-dehydration calculated salinities, porosity, and gravimetric water content (m_{fluid}/m_{solid}) for all the SIP-measured clay samples.

Initial Salinity	(D.water)	(10^{-3} M NaCl)	(10^{-2} M NaCl)	(10^{-1} M NaCl)	(1 M NaCl)
Clay type	Final salinity (M NaCl)				
Kaolinite sample	D.W.	1.53×10^{-3}	1.54×10^{-2}	1.91×10^{-1}	1.76
Illite sample	D.W.	1.92×10^{-3}	1.80×10^{-2}	1.82×10^{-1}	1.91
Green Montmorillonite sample	D.W.	1.39×10^{-3}	1.53×10^{-2}	1.46×10^{-1}	1.54
Red Montmorillonite sample	D.W.	1.64×10^{-3}	1.71×10^{-2}	1.54×10^{-1}	1.51
Clay type	Porosity	Porosity	Porosity	Porosity	Porosity
Kaolinite sample	0.54	0.59	0.57	0.56	0.47
Illite sample	0.52	0.56	0.54	0.56	0.42
Green Montmorillonite sample	0.65	0.68	0.68	0.71	0.57
Red Montmorillonite sample	0.67	0.62	0.61	0.62	0.51
Clay type	Water content				
Kaolinite sample	0.48	0.51	0.55	0.54	0.44
Illite sample	0.49	0.41	0.46	0.43	0.40
Green Montmorillonite sample	1.02	0.96	0.91	0.93	0.85
Red Montmorillonite sample	0.71	0.63	0.60	0.66	0.67

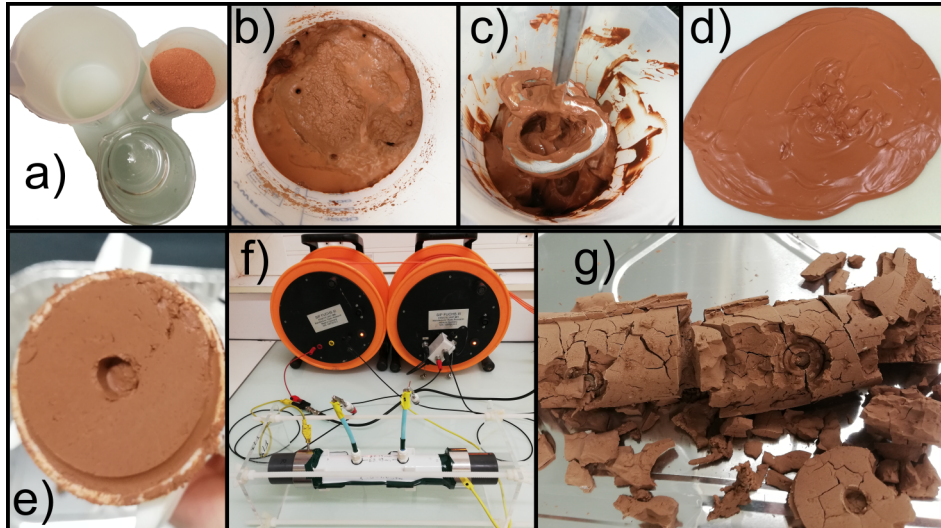


Figure 2. Laboratory protocol to create clay samples: a) Combination of clay powder and water. b) Saturation of clay powder for at least 24 h. c) Homogenization of mixture with drill. d) Excess water evaporation until correct plasticity is reached. e) Setting clay in sample holder. f) SIP measurements. g) Clay sample drying.

330 through optic cables to reduce electromagnetic noise. The SIP-FUCHS III outputs the
 331 amplitude of the measured impedance (Ω), the phase shift between injected and mea-
 332 sured signal (mrad), and their respective errors, for each measured frequency.

333 The current electrodes C1 and C2 are stainless steel cylinders that we use also as cov-
 334 ers for the sample holder, while we use home-made non-polarizable electrodes for P1 and
 335 P2. We made our own Cu-CuSO₄ non-polarizable electrodes, following the procedure
 336 proposed by Kremer et al. (2016). They consist of a copper wire inserted in a plastic tube
 337 filled with a saturated solution of copper sulfate and gelatin, plugged by a porous filter
 338 at the bottom. We used a near cylindrical sample holder of length 22.9 cm and radius
 339 2.1 cm, with electrode separation of 7.4 cm, that is separated roughly by a third of the
 340 sample holder's total length (Figure 3b); this pseudo-Wenner configuration has been used
 341 previously by Ghorbani et al. (2009), and Jougnot et al. (2010). The geometrical fac-
 342 tor to convert measured impedances to conductivities has been determined using finite
 343 elements numerical methods, this approach has been used previously by Jougnot et al.
 344 (2010).

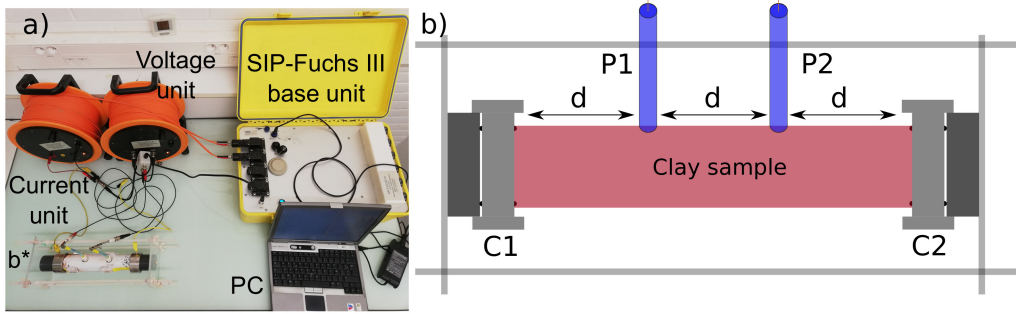


Figure 3. a) Laboratory set-up for SIP measurements on our clay samples with the sample holder, injecting and measuring units (orange), SIP-FUCHS III, and a computer to store the data. b) Sample holder sketch with the external structure. C1 and C2 are two cylindrical plates, our current electrodes that inject a sinusoidal electric current. P1 and P2 are a pair of non-polarizable electrodes that measure the resulting electrical potential difference, they are equally distanced from the current electrodes, making a pseudo-Wenner array.

345 We created an external structure to hold the sample holder (Figure 3b) in order to achieve
 346 repeatability in our measurements. Indeed, we needed the ability to close the sample holder
 347 at the exact same position and with the same pressure between measurements. As re-
 348 peatability test, we built two identical sample holders, made two individual green mont-
 349 morillonite samples, and measured the SIP signal in both samples. The repeatability of
 350 the measurements shows a 4.7% difference on the real part of the electrical conductiv-
 351 ity and a 0.47% difference on the imaginary part at 1.46 Hz. For the whole spectrum,
 352 we see a maximum percentage difference of 4.8% on the real part of the electrical con-
 353 ductivity (at 2.9 mHz) and 11.89% for the imaginary part (at 45.8 mHz). In average,
 354 for the whole spectrum, we see a difference of 4.6% for the real part of the spectrum, and
 355 1.5% for the imaginary part. See the supplementary information file, to visualize the re-
 356 peatability test. We acknowledge that the difference between the real part of the con-
 357 ductivity between both samples is surprising (although negligible). We think that such
 358 difference lies on the fact that we are dealing with two different clay samples in two dif-
 359 ferent sample holders. A minimal difference between these two will correspond to a min-
 360 imal difference between their signals.

3.4 Optimization of the double-Pelton model

For the optimization procedure, we use our SIP data as input, that is, conductivity amplitude (S m^{-1}) and phase (rad), and then fit a double-Pelton model (see equation 6). In this paper, we optimize for seven parameters: ρ_0 , m_1 , m_2 , τ_1 , τ_2 , c_1 , and c_2 . The cost function is:

$$\Phi = \frac{\sum_{i=1}^{N_a} (A_{mes}^i - A_{mod}^i)^2}{\sum_{i=1}^{N_a} (A_{mes}^i - \langle \mathbf{A}_{mes} \rangle)^2} + \frac{\sum_{i=1}^{N_p} (P_{mes}^i - P_{mod}^i)^2}{\sum_{i=1}^{N_p} (P_{mes}^i - \langle \mathbf{P}_{mes} \rangle)^2}, \quad (8)$$

where, A_{mes} represents the measured amplitude vector, $\langle \mathbf{A}_{mes} \rangle$ represents the mean of the measured amplitude vector, A_{mod} , the modeled or calculated amplitude vector, via the double-Pelton model, N_a is the number of amplitude data points that have been preserved, P_{mes} is the measured phase vector, $\langle \mathbf{P}_{mes} \rangle$ is the mean of the measured phase vector, P_{mod} is the modeled or calculated phase vector, and N_p is the number of phase data points that have been kept. The strategy we used was to first optimize with a simulated annealing approach, that has been explained in detail in Maineult (2016). For the parameters m_1 , m_2 , c_1 , and c_2 , we let them vary between [0 - 1], for ρ_0 we usually use $[\bar{\rho} \pm (0.2 \cdot \bar{\rho}) \Omega \cdot m]$, for τ_1 we usually use $[10^{-3} - 10^6]$ s, and finally for τ_2 we use $[10^{-10} - 10^1]$ s. Here, $\bar{\rho}$ is the arithmetic mean electrical resistivity for all frequencies. We later optimize the double-Pelton parameters using a simplex optimization procedure (Caceci & Cacheris, 1984). This same strategy has been used in Maineult et al. (2017). As input of the simplex code we use our measured SIP data (amplitude and phase) and as initial model we use the result of the simulated annealing method. The simulated annealing step allows us to explore the parameter space preventing to get trapped in a local minimum, but this is done in a discrete manner. When we know the vicinity of the solution, we use the Simplex optimization procedure to refine the solution.

Moreover, we fixed a double-Warburg model for the red and green montmorillonite samples, as well as the kaolinite sample. A double-Warburg model is a double-Pelton model but with $c_1 = 0.5$ and $c_2 = 0.5$. In the case of these three types of clay samples, we turned the optimization code and obtained values of c_1 and c_2 near 0.5. Therefore, we opted that for these three types of clay samples, we would fix c_1 and c_2 , and we would only optimize for the remaining five parameters, that is: ρ_0 , m_1 , m_2 , τ_1 , and τ_2 . It is worth mentioning, that we tried fixing c_1 and c_2 for the illite sample as we also obtained val-

ues near 0.5, but we obtained poor fits with $c_1 = 0.5$ and $c_2 = 0.5$. We assume then that the illite sample does not behave as a double-Warburg, but as a double-Pelton. The rest of the clay samples (kaolinite, red and green montmorillonite samples) do behave as double-Warburg models. The results of our fits are presented later on in this article, in Table 4.

3.5 Differentiation of clay minerals

In order to compare our SIP datasets, we calculated the normalized measured conductivity differences ($\Delta\sigma_N^*$) between each clay type for every salinity at 1.46 Hz, for both the real and imaginary parts of the complex conductivity. We chose 1.46 Hz because frequencies near 1 Hz represent a classic choice in geophysics (Zanetti et al., 2011). Also, as it will be presented in the results and discussion sections, the peak polarization phenomena happens near 10^0 Hz. To choose this particular frequency, we also took into account that the highest measured errors in the data happened at the lowest frequencies (mHz range), because less stacking is possible, due to the long time periods for each measurement. The noisiest data happened at the highest frequencies (kHz range). Indeed, according to Huisman et al. (2016) the electromagnetic coupling effects happen at the highest frequency range of our SIP measurements, in the kHz range. Therefore, when choosing near 1 Hz, we should get the most accurate data. We calculate $\Delta\sigma_N^*$ values between each clay type at 1.46 Hz, for the datasets shown in Figure 4. To calculate the $\Delta\sigma_N^*$ we use:

$$\Delta\sigma_N^*(f = 1.46 \text{ Hz}) = 100 \times \frac{\sigma_1^* - \sigma_2^*}{\frac{\sigma_1^* + \sigma_2^*}{2}}, \quad (9)$$

where σ_1^* and σ_2^* represent the complex conductivity value at 1.46 Hz of an individual type of clay. The idea is to quantify if we are able to distinguish between two different clay minerals in a laboratory setting. That is, if the $\Delta\sigma_N^*$ value is low (e.g. below 10%) that means we are hardly able to differentiate two specific clay minerals at the laboratory scale, then at the field scale it would seem impossible to differentiate such clay minerals. Conversely, if we have a high $\Delta\sigma_N^*$ (e.g. above 100%) it would not mean that we could automatically differentiate two different clay minerals at the field scale.

417 4 Results

418 We obtained a large SIP dataset in the laboratory. To make our interpretation of
 419 this dataset more accessible, we decomposed their analysis into several subsections. First,
 420 we will present the complex conductivity values at 1.46 Hz vs. the calculated water con-
 421 ductivity, to get a quick view of the electric behavior of the clay samples at varying salin-
 422 ities. After that, we present the normalized spectrum of the real part of the complex con-
 423 ductivity per clay type; we show the evolution with salinity. We then present the full spec-
 424 tra of the complex conductivity for all clay samples and all salinities. Afterwards, we present
 425 the results of our double-Pelton fits, and the obtained parameters. We finally present
 426 a quantitative differentiation between clay samples at the same salinity. We filtered all
 427 of our datasets with a 5% percent filter. That is, if the error of the measured amplitude
 428 is larger than 5%, we remove the data point from our dataset. We performed our SIP
 429 measurements at five salinities on four types of clay: montmorillonite samples (red and
 430 green), a kaolinite sample and an illite sample (see Table 2). Additionally, we performed
 431 SIP measurements at three salinities (initially de-ionized water, 1×10^{-2} , and 1 M of
 432 NaCl) on two extra types of clay: beige montmorillonite sample and a Boom clay sam-
 433 ple. Boom clay is a natural clayrock used for nuclear waste storage (Ortiz et al., 2002).
 434 The results of these additional types of clay are shown as supplementary information in
 435 this article.

436 4.1 Results at varying salinities at 1.46 Hz

437 We collected SIP measurements of four different types of clay (red and green mont-
 438 morillonite samples, an illite sample, and a kaolinite sample) with the SIP-FUCHS III.
 439 We used frequencies from 10^{-3} to 10^4 Hz. The calculated water conductivity values (fol-
 440 lowing equation 7) presented in Figure 4, correspond to those of the post-dehydration
 441 salinities (Figure 2d and e). We chose to present the data points at 1.46 Hz, because the
 442 highest measured errors and the noisiest data are present at the lowest and highest fre-
 443 quencies, respectively. It should be noted that the low salinity (initially 10^{-3} M NaCl)
 444 simulated water conductivity values may be underestimated because we did not consider
 445 clay dissolution as well as cation leaching from the interlayer space of montmorillonite.
 446 In Figure 4a we observe that the real conductivity increases with an increase in the con-
 447 ductivity of the fluid saturating our clay mixtures for all salinities for all types of clay.

448 In addition, Figure 4a shows that both montmorillonite samples exhibit higher surface
 449 conductivity than the illite and kaolinite samples. Due to their difference in surface elec-
 450 trical properties (see section 2.1), it is a bit surprising to see that the kaolinite and il-
 451 lite samples may have the same surface conductivity here. This may be due to the fact
 452 that the kaolinite sample is not pure and contains 4% in weight of more conducting smec-
 453 tite.

454 With the imaginary conductivity we see a different behavior. For the red and green mont-
 455 morillonite samples, we see a peak of the imaginary conductivity at the second to high-
 456 est salinity (corresponding to a water conductivity in the 10^0 S m⁻¹ range). For the kaoli-
 457 nite and illite samples, we see a similar behavior, however, we see the peak in the range
 458 of 10^{-1} S m⁻¹ for the water conductivity. The imaginary conductivity amplitude is also
 459 roughly one order of magnitude higher for the montmorillonite samples than for other
 460 clay samples. Due to their higher CEC and stronger EDL, the montmorillonite samples
 461 polarize more than the illite and kaolinite samples. In addition, the zeta potential of Na-
 462 montmorillonite in a NaCl solution is higher in magnitude than the zeta potential of il-
 463 lite and kaolinite in a NaCl solution (Sondi et al., 1996; Leroy & Revil, 2004; Leroy et
 464 al., 2015). Consequently, membrane polarization effects may be higher for Na-montmorillonite
 465 than for illite and kaolinite. It results that more salt is necessary to decrease the imag-
 466 inary conductivity of montmorillonite compared to illite and kaolinite at high salinity.
 467 Note that although we collected SIP data at five different salinities, the de-ionized wa-
 468 ter dataset are not presented in Figure 4. We chose not to present those data points be-
 469 cause knowing or controlling the conductivity of the pore water at that salinity proved
 470 to be very complex, and out of the scope of this paper. However, the datasets of de-ionized
 471 water are presented in the following parts of this paper.

472 Equation 2 was adjusted to the σ' values at 1.46 Hz (for 10^{-3} -1 M NaCl) by consider-
 473 ing that the formation factor and the surface conductivity are independent from the pore
 474 water conductivity. For this adjustment, more weight was attributed to the values for
 475 the two highest pore water conductivities as they are expected to be less sensitive to the
 476 surface conductivity (see Weller et al., 2013). This procedure provides a single surface
 477 conductivity per sample presented in Table 3 and seems to overestimate its values for
 478 the lowest pore water conductivity. As expected, we see larger values of σ'_{surf} for both
 479 montmorillonite samples, because these clay samples have a more important surface elec-
 480 tric charge and specific surface area than the illite or kaolinite samples. We recognise the

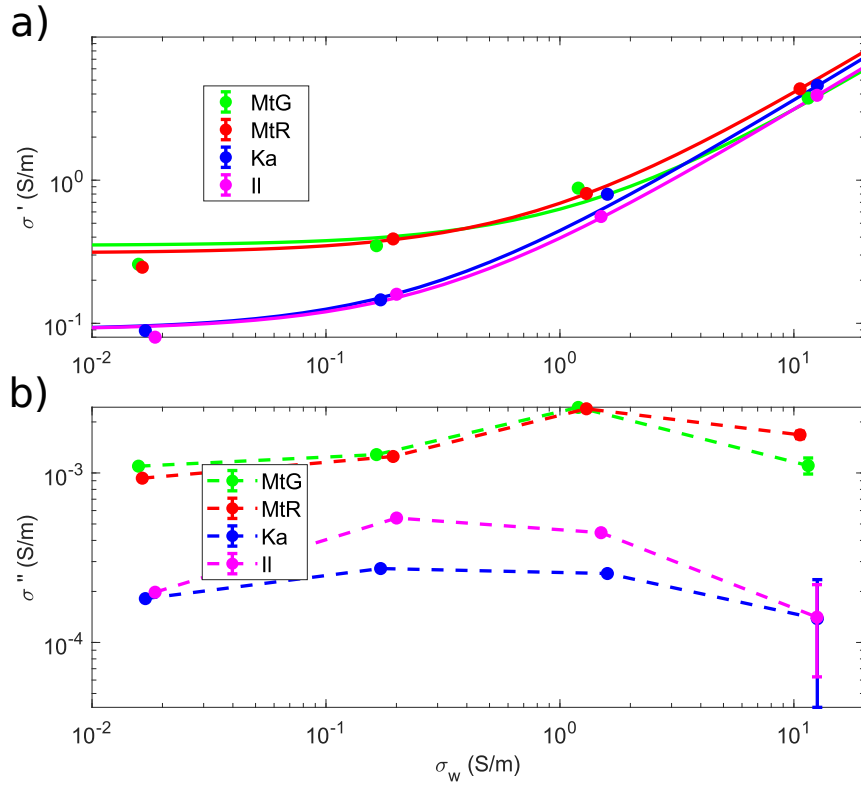


Figure 4. Measured (points) real (a) and imaginary (b) conductivity of the four clay samples as a function of simulated water conductivity, at a frequency of 1.46 Hz. MtG represents the green montmorillonite sample, MtR the red montmorillonite sample, Ka the kaolinite sample, and Il the illite sample. The bold line on (a) is the calculated $\sigma'(\sigma_w)$ from equation 2, the parameters we fit are presented in Table 3.

Table 3. Formation factors (F) and σ'_{surf} fitted from equation 2 for the values at 1.46 Hz, CEC and specific surface area (Ss) of the clay samples.

Clay type	F [-]	σ'_{surf} [Sm^{-1}]	CEC [meq/100 g]	Ss* [m^2/g , BET]
Kaolinite sample	2.82	0.09	22	16.94
Illite sample	3.29	0.09	47	101.60
Green mont. sample	3.60	0.35	132	77.71
Red mont. sample	2.63	0.31	135	71.09

*Specific surface measured through the BET (Brunauer-Emmett-Teller) method for each sample. BET cannot probe the interlayer space of montmorillonites.

481 formation factor values we obtained have some uncertainty and are only meant as a mean
 482 of the electrical formation factor for each type of clay sample, as we are dealing with clay
 483 muds with varying porosities and not hard rocks with a specific formation factor. We
 484 present the σ' calculated values from the σ'_{surf} and F fitted values in Figure 4a. It is
 485 worth mentioning that the specific surface areas measured using the BET (Brunauer-
 486 Emmett-Teller) technique might not be representative of the true values for the mont-
 487 morillonites mineral. Indeed, previous work from the literature indicate this technique
 488 is not able to properly probe interlayer space (Tournassat et al., 2003; Hassan et al., 2006,
 489 e.g.,). In order to do so, other methods such as wet-state methylene blue (MB) should
 490 be used Weller et al. (2015a). Another possibility to better determine the real specific
 491 surface area could be through a calculation of the specific surface area based on the XRD
 492 characterisation of the samples. According to the literature the specific surface area of
 493 montmorillonites should be in the range of 390-780 m^2/g (see Tournassat et al., 2013).

494 4.2 Normalized real conductivity

495 In Figure 5 we show the normalized real conductivity for all clay samples. For nor-
 496 malization value we used the amplitude of the conductivity at 1.46 Hz, per clay type,
 497 per salinity. We observe that overall the signal of the normalized real conductivity gets

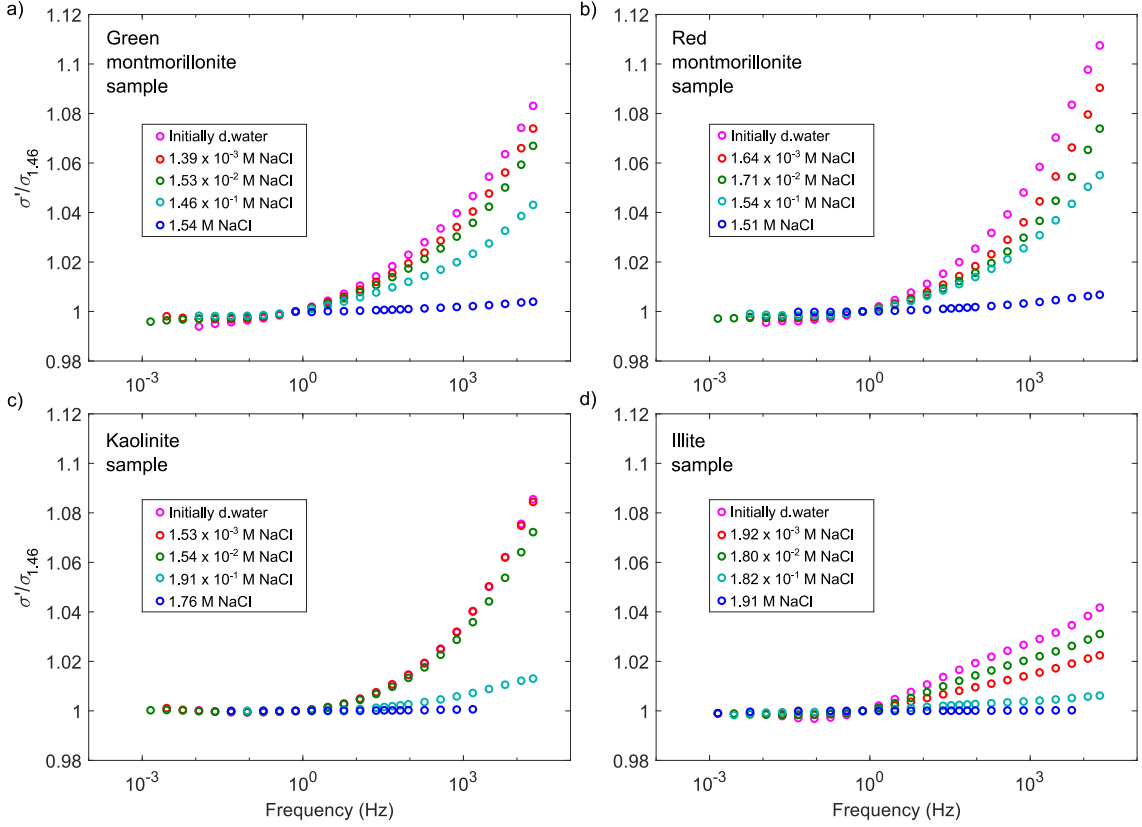


Figure 5. Normalized real conductivity for all salinities per clay type: a) green montmorillonite sample, b) red montmorillonite sample, c) kaolinite sample, and d) illite sample. All these spectra have been normalized by the conductivity amplitude at 1.46 Hz.

498 flattened as the salinity increases. In other words, we see less of a change in the normal-
 499 ized real conductivity within the measured frequency range as the salinity of the fluid
 500 increases. We interpret this as evidence that at the highest salinity, pore conduction dom-
 501 inates over the surface conduction, and we are able to see this evolution with salinity.
 502 The normalized value presented in Figure 5 could be interpreted as a ratio of alternat-
 503 ing current (AC) conduction vs. close to direct current (DC) conduction. Even though
 504 we see an overall decrease with salinity of $\sigma'/\sigma_{1.46}$. This decrease could be interpreted
 505 as evidence that the DC conduction increases faster with salinity than the AC conduc-
 506 tion due to polarization. We used a frequency of 1.46 Hz as normalization value because,
 507 as mentioned previously in the paper, it is a classic choice in geophysics. Also, in field
 508 geophysics, the usual frequency utilized by electrical instruments is around 1 Hz, and those
 509 measurements (i.e. electrical resistivity tomography) are thought of as DC measurements.
 510 A true DC value would make use of the lowest measured frequency.

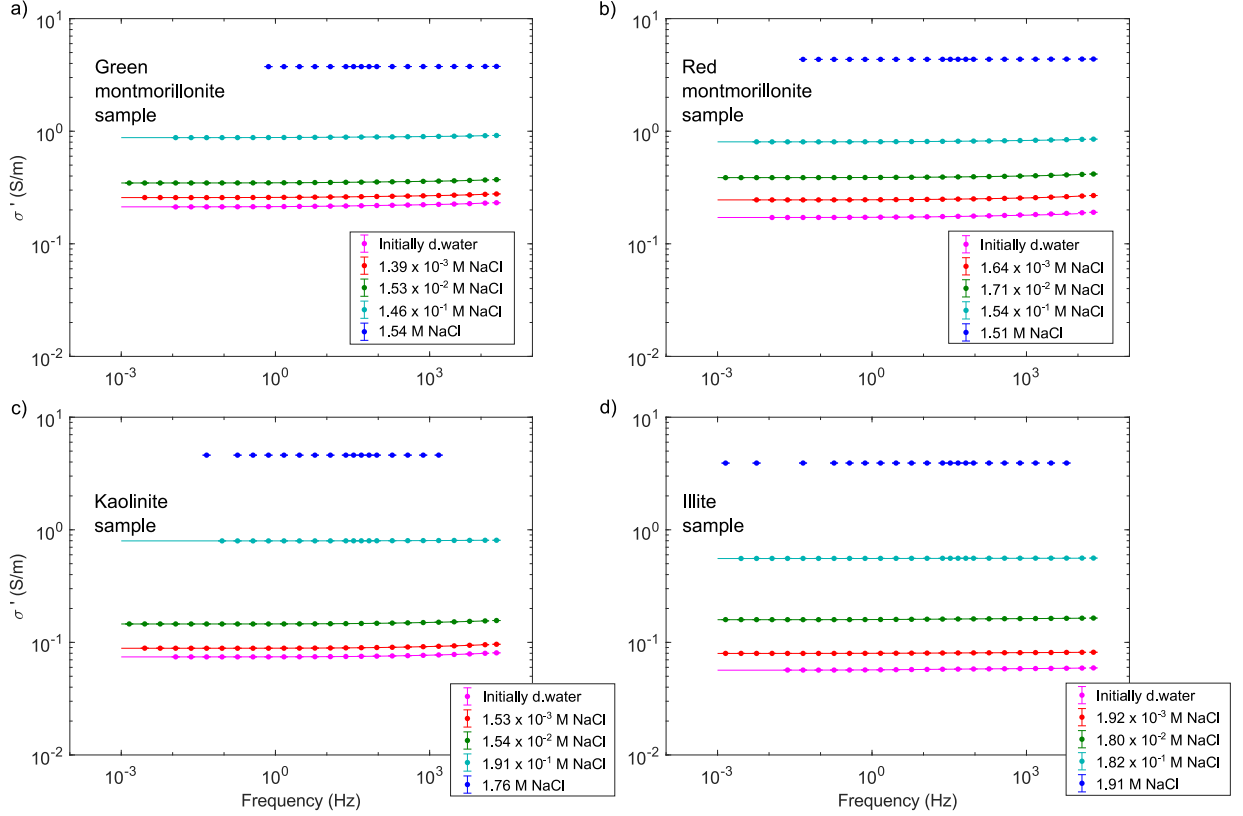


Figure 6. Real part of the complex conductivity per salinity of: a) green montmorillonite sample, b) red montmorillonite sample, c) kaolinite sample, and d) illite sample. The calculated salinity values at which the SIP measurements were collected are presented in the legends of each subplot. Dots with errorbars represent the measured SIP data, and the line represents the double-Pelton model predictions for each dataset.

511 **4.3 Effect of the salinity on the spectra**

512 Figure 6 shows the real conductivity spectra of each clay per salinity, with the double-
 513 Pelton model superimposed onto the dataset. We see for all of the clay samples that as
 514 the salinity increases, the real conductivity also increases. We do however notice that
 515 the data seems more dispersed for the kaolinite and illite samples, meaning, the differ-
 516 ence between maximum and minimum conductivities seems bigger for the kaolinite and
 517 illite samples, than for the montmorillonite samples.

518 Figure 7 shows the imaginary conductivity spectra of each clay per salinity, with the double-
 519 Pelton model predictions superimposed onto the dataset. For the montmorillonite sam-
 520 ples we see the overall highest polarization at the second to highest salinity. Finally, for

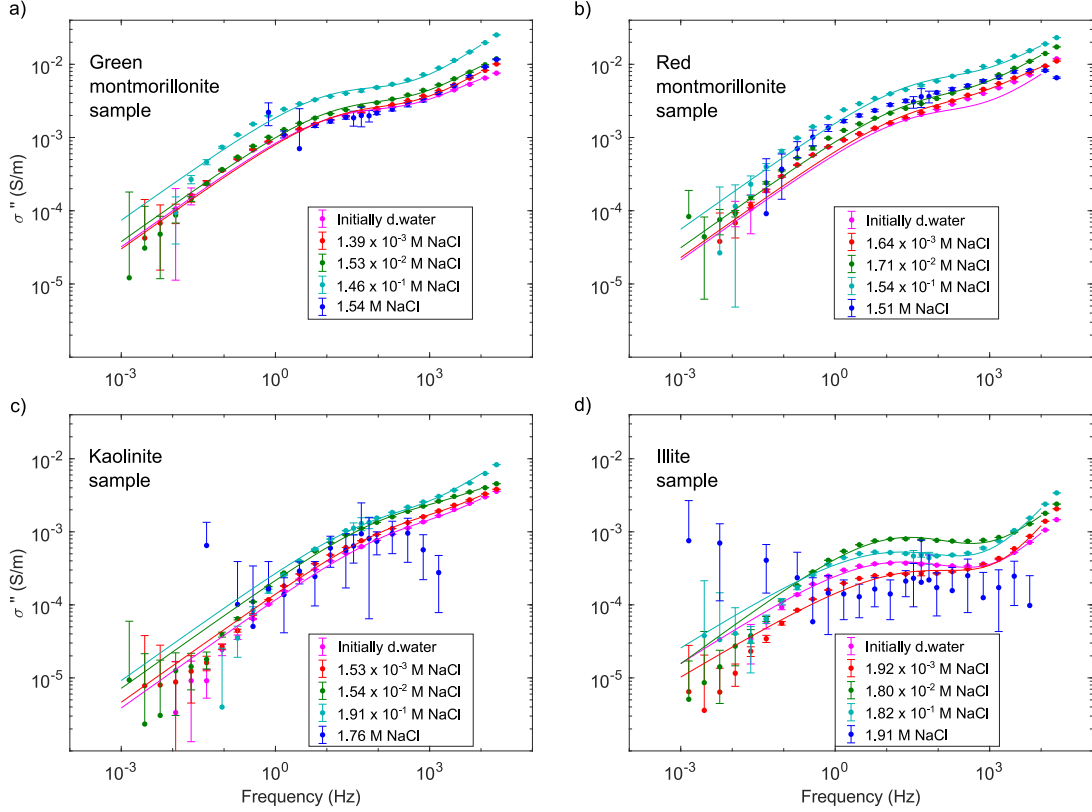


Figure 7. Imaginary part of the complex conductivity per salinity of: a) green montmorillonite sample, b) red montmorillonite sample, c) kaolinite sample, and d) illite sample. The calculated salinity values at which the SIP measurements were collected are presented in the legends of each subplot. Dots with errorbars represent the measured SIP data, and the line represents the double-Pelton model predictions for each dataset.

521 the kaolinite and illite samples, we see the highest polarization at the middle salinity (10^{-2}
 522 M of NaCl salinity range), this is better seen for the illite sample.

523 The errorbars become larger in the highest salinity measurements. This is expected from
 524 the measurement itself. Indeed, measuring low phases, that is very small time differences
 525 between the injected current and the resulting voltage signal, is a real challenge for the
 526 electronics involved in SIP measurements (Zimmermann et al., 2008). Nevertheless, it
 527 is possible to distinguish a clear tendency with frequency, in most of the spectra, except
 528 for the illite and kaolinite samples at the highest salinity.

529 **4.4 Double-Pelton model fits and variation of Pelton parameters with**
 530 **varying salinities**

531 In Figure 8 we present the principle of the double-Pelton model decomposition. We
 532 sum two individual Pelton signals (see equation 6), the resulting signal is the one that
 533 we fit our data with. It is worth mentioning that we use the filtered data for this pro-
 534 cess. We assume that the high frequency peak (in blue) happens due to partly an induc-
 535 tive and capacitive effect (Huisman et al., 2016) plus polarization of the clay (Leroy &
 536 Revil, 2009; Okay et al., 2014; Leroy et al., 2017). We assume that the mid-frequency
 537 peak (in red) corresponds solely to the polarization of clay.

538 In Table 4 we have summarized the optimized Pelton parameters of both the red and
 539 blue peaks (Figure 8). Furthermore, as mentioned previously, we used a double-Warburg
 540 model ($c_1=0.5$ and $c_2=0.5$) for all clay samples except the illite sample, that was fitted
 541 with a double-Pelton (fitted c_1 and c_2). We present fully the double-Pelton parameters
 542 as we believe it will be of interest to the community to have access to Pelton param-
 543 eters of individual types of clays at varying salinities, for possible forward-modeling op-
 544 portunities.

545 For the four lowest salinity datasets, we observe how at the highest fitted salinity, there
 546 is a considerable decrease in the chargeability (m_1) parameter for the lower frequency
 547 local maxima. For all datasets we see chargeability values (in each individual local max-
 548 ima) in the same magnitude order. We also see an increase on DC electrical conductiv-
 549 ity with increasing salinity, as expected. Note that we present values of electrical con-
 550 ductivity, instead of resistivity (as shown in the double-Pelton model, equation 6), as the
 551 complex conductivity is only the inverse to the complex resistivity. As for the illite sam-
 552 ple, we see that for c_1 all values linger near 0.5, but not quite 0.5. Finally, we see that
 553 the relaxation times for the second (high frequency) local maxima are mostly below the
 554 μs range, and that for the second local maxima, these are considerably above.

555 **4.5 Differentiation of clay minerals**

556 After calculating the $\Delta\sigma_N^*$ (equation 9), we see that the values of the $\Delta\sigma_N^*$ for the
 557 real part decrease with increasing salinities overall, agreeing with what we observe in Fig-
 558 ure 5, for the normalized real conductivity. This behavior is not so clear or evident for
 559 the imaginary part. We also observe that the $\Delta\sigma_N^*$ value is smaller between the mont-

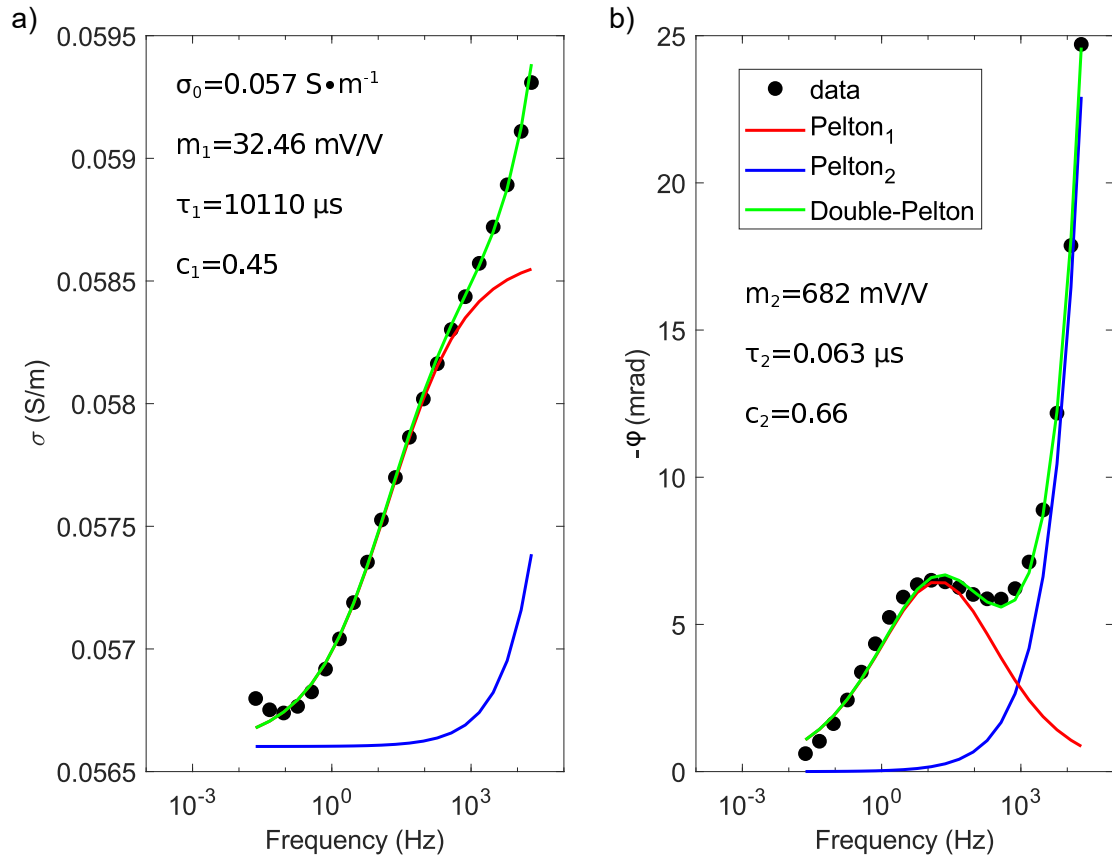


Figure 8. Fit of a double-Pelton model (equation 6) to our data, in both a) amplitude and b) phase. We present the illite sample dataset using initial de-ionized water (points), and the corresponding double-Pelton model (green line), with two individual Pelton models (blue and red lines).

Table 4. Double-Pelton parameters obtained from the optimization procedure of section 3.4 to reproduce SIP signal on the four studied clay types.

Clay type	Salinity [M NaCl]	σ_0 [S m ⁻¹]	m_1 [mV/V]	τ_1 [μ s]	c_1	m_2 [mV/V]	τ_2 [μ s]	c_2	RMS [-]
Kaolinite	D.W.	0.074	40.14	333	0.5	345	0.327	0.5	1.78×10^{-3}
	1.53×10^{-3}	0.089	40.68	332	0.5	249	0.599	0.5	1.82×10^{-3}
sample	1.54×10^{-2}	0.146	34.86	413	0.5	142	1.483	0.5	1.52×10^{-3}
	1.91×10^{-1}	0.797	5.66	842	0.5	350	0.014	0.5	2.63×10^{-2}
Illite	D.W.	0.057	34.26	10110	0.45	682	0.063	0.66	4.82×10^{-3}
	1.92×10^{-3}	0.080	20.00	3261	0.42	740	0.143	0.84	5.26×10^{-3}
sample	1.80×10^{-2}	0.159	22.57	7662	0.51	515	0.021	0.56	6.18×10^{-3}
	1.82×10^{-1}	0.557	5.11	10369	0.44	342	0.043	0.76	7.21×10^{-3}
Green mont.	D.W.	0.213	37.40	4418	0.5	158	1.917	0.5	4.75×10^{-3}
	1.39×10^{-3}	0.257	32.55	3432	0.5	249	0.56	0.5	4.23×10^{-3}
sample	1.53×10^{-2}	0.347	28.27	3957	0.5	198	0.803	0.5	2.72×10^{-3}
	1.46×10^{-1}	0.877	18.48	5758	0.5	504	0.052	0.5	3.87×10^{-3}
Red mont.	D.W.	0.171	42.32	2266	0.5	958	0.048	0.5	9.61×10^{-2}
	1.64×10^{-3}	0.245	30.87	2046	0.5	200	1.88	0.5	3.78×10^{-3}
sample	1.71×10^{-2}	0.387	27.47	2033	0.5	306	0.452	0.5	3.85×10^{-3}
	1.54×10^{-1}	0.805	25.76	1846	0.5	188	0.528	0.5	7.41×10^{-3}

560 morillonite samples, as expected, that is the montmorillonite samples are electrically sim-
 561 ilar to each other. For the lowest salinity (initially de-ionized water) the biggest differ-
 562 ence in real conductivity is between the illite and the green montmorillonite samples (-116% ,
 563 the real conductivity of the illite sample is smaller than that of the montmorillonite sam-
 564 ple), and for the imaginary part it is between the kaolinite and the green montmorillonite
 565 samples (-149% , the imaginary conductivity of the kaolinite sample is smaller than that
 566 of the montmorillonite sample). For the initial 10^{-3} M salinity (NaCl) the biggest dif-
 567 ference in real conductivity is between the illite and the green montmorillonite samples
 568 (-105%), and for the imaginary part it is between the kaolinite and the green montmo-
 569 rillonite samples (-143%). For the initial 10^{-2} M salinity, the biggest difference in real
 570 conductivity is between the kaolinite and the red montmorillonite samples (-91%), and
 571 for the imaginary part it is between the kaolinite and the green montmorillonite sam-
 572 ples (-130%). For the initial 10^{-1} M salinity, the biggest difference in real conductiv-
 573 ity is between the illite and the green montmorillonite samples (-45%), and for the imag-
 574 inary part it is between the kaolinite and the green montmorillonite samples (-162%).
 575 For the highest salinity, the biggest difference in real conductivity is between the kaoli-

Table 5. $\Delta\sigma_N^*$ (in %) for the initially 10^{-2} M of NaCl clay mixtures. These calculations are made using the complex conductivity at 1.46 Hz, the real part is on the lower left triangle (in bold), and the imaginary part is on the upper right triangle (in italics). MtG represents the green montmorillonite sample, MtR the red montmorillonite sample, Ka the kaolinite sample, and IL the illite sample.

	MtG	MtR	Ka	IL
MtG	0	<i>2.56</i>	<i>129.84</i>	<i>81.20</i>
MtR	10.85	0	<i>128.34</i>	<i>79.06</i>
Ka	-82.00	-90.83	0	<i>-66.04</i>
IL	-74.37	-85.53	9.01	0

576 nite and the green montmorillonite samples (20%), and for the imaginary part it is be-
577 tween the kaolinite and the red montmorillonite samples (-169%). Table 5 presents the
578 $\Delta\sigma_N^*$ values for the initial salinity of 10^{-2} M of NaCl. We use σ_1 (see equation 9) as the
579 value of the column, and σ_2 of the row. For example, in Table 5, we obtained 10.85, us-
580 ing the σ' of the red montmorillonite sample as σ_1 , and of the green montmorillonite sam-
581 ple as σ_2 (see equation 9). The lower left triangle corresponds to calculation for the real
582 part of the complex conductivity (in bold), and the upper right triangle corresponds to
583 the imaginary part (in italics). The tables for the rest of the salinities are presented in
584 the supplementary information part of this paper.

585 5 Discussion

586 In this study we propose a new experimental protocol with verified repeatability
587 to characterize the complex electrical conductivity spectra of non-consolidated clay sam-
588 ples. We obtain a unique SIP dataset composed of four types of clay samples and sat-
589 urated by a NaCl solution at five different salinities. We first interpreted the dataset at
590 1.46 Hz for the real and imaginary parts of the electrical conductivity before studying
591 the entire spectra and fitting them with a double-Pelton phenomenological model, and
592 presenting a schematic figure on how we interpret the polarization phenomena of our re-
593 sults.

594 Our measurements, at 1.46 Hz (Figure 4b), show that the quadrature conductivity (imag-
595 inary part of the complex conductivity) hits a maximum at a certain salinity and then
596 decreases. The salinity at which this maximum exists depends on the type of clay. For
597 the kaolinite and the illite samples, we have the maximum at the mid-salinity (around
598 10^{-2} M of NaCl salinity range), while it is a higher salinity for the montmorillonite sam-
599 ples (around 10^{-1} M of NaCl). It should be noted that we do not have the exact salin-
600 ity at which the maximum quadrature conductivity happens because we investigated 5
601 finite salinities, that is, perhaps the maximum of the quadrature happens between two
602 of our measured salinities. Among the published SIP dataset on clay samples, Vinegar
603 & Waxman (1984) present an extense dataset of the complex electrical conductivity from
604 21 shaly sands, measured at 4, 5 or 7 different salinities (0.01, 0.05, 0.1, 0.25, 0.5, 1.0,
605 and 2.0 M NaCl); see Tables 1 and 2 of Vinegar & Waxman (1984). Some of their sam-
606 ples also exhibit the behavior with a maximum quadrature conductivity at a particular
607 salinity, notably the samples with more shale content. They propose that the decrease
608 of the quadrature conductivity happens due to a decrease of the membrane effect. Weller
609 et al. (2010) proposed that the relationship between the imaginary part and the water
610 conductivity is guided by the specific surface area. For this, they analyzed IP or SIP data
611 from 114 samples, including sandstones, and sand and clay mixtures. Revil & Skold (2011)
612 also present a dataset composed of 7 samples of sandstones and unconsolidated sand from
613 the literature where most of the datasets present the same trend where a maximum in
614 quadrature conductivity appears at a particular salinity. The behavior shown in Figure
615 4b is also consistent with the one reported by Weller & Slater (2012), both share the same
616 water conductivity range. They measured SIP on 67 samples of sandstones and uncon-
617 solidated sediments. Okay et al. (2014) measured SIP on bentonite and kaolinite quartz
618 sand mixtures, at different clay contents 100%, 20%, 5%, and 1%. They present the be-
619 havior of the quadrature conductivity with respect to water conductivity, at only three
620 NaCl salinities. Their bentonite samples (95% smectite content) and kaolinite samples
621 (15% smectite content) present an increase in the quadrature conductivity with salin-
622 ity; the maximum water conductivity presented is around 1.5 S/m. Finally, Lévy et al.
623 (2019b) measured the SIP response of a set of 88 volcanic altered rocks with varying amounts
624 of smectite. They present the SIP spectra from four of their samples (Figure 1 in Lévy
625 et al., 2019b), using four different fluid conductivities, 0.04, 0.1, 0.5, and 1.5 S m⁻¹ (from
626 four different NaCl concentrations). They show an overall increase in polarization (quadra-

627 ture conductivity) with salinity for these four samples. If we only analyze the smectite
 628 samples of our dataset, we see a progressive increase in the quadrature conductivity with
 629 increase of fluid conductivity, until we reach the highest salinity, where we see a decrease
 630 (see Figure 4b). Only one of the samples presented with the full conductivity spectra (Fig-
 631 ure 1 in Lévy et al., 2019b) has more than 20 % smectite. If we only take a look at this
 632 sample, it doesn't show a decrease in quadrature conductivity with the highest salinity,
 633 although, their highest presented pore water conductivity for this data subset is 1.5 S m^{-1}
 634 m^{-1} . For the smectite samples of our dataset, we see a decrease on the quadrature con-
 635 ductivity just at the highest pore water conductivity, around 10 S m^{-1} . According to
 636 these studies, it is interesting to notice that the increase of the quadrature conductiv-
 637 ity with salinity is larger for sandstones and quartz sand than for smectite minerals. This
 638 observation confirms the assumption that the quadrature conductivity of these materi-
 639 als is directly sensitive to their surface charge controlling EDL polarization (Okay et al.,
 640 2014; Leroy et al., 2017). Indeed, the surface charge of quartz strongly increases with
 641 pH and salinity due to the deprotonated silanol surface sites whereas the smectite min-
 642 erals carry a permanent negative surface charge less sensitive to pH and salinity on their
 643 basal surface due to isomorphic substitutions in the crystal lattice. Weller & Slater (2012)
 644 suggest further investigation at even higher salinities, this could be important for high
 645 salinity environments, such as oceanic shale reservoirs (Morsy & Sheng, 2014). Due to
 646 such a high electrical conductivity of such sample, the SIP measurement logistics could
 647 be complex, and better protocols and measuring equipment with good uncertainty at high
 648 conductivities are needed.

649 Furthermore, Weller et al. (2013), Woodruff et al. (2014), and Lévy et al. (2019b) ob-
 650 served a linear relation between σ''_{surf} and σ'_{surf} . Weller et al. (2013) used a database
 651 composed of 63 sandstones and unconsolidated sediment samples. They overall found
 652 the linear parameter (l) of equation 5 to be 0.042. Woodruff et al. (2014) worked on a
 653 variety of shales, and found $l = 0.022$ for their dataset, they call it parameter R in their
 654 work. In addition, Lévy et al. (2019b) studied a variety of volcanic rocks, with different
 655 smectite contents, and they found that the linear relation between σ''_{surf} and σ'_{surf} de-
 656 creases in magnitude with smectite content. They calculate $l = 0.002$ for a data sub-
 657 set with more than 20% smectite content. According to Revil (2012), this very low l value
 658 of samples with high smectite content compared to the l value of sandstones and uncon-
 659 solidated sediment samples may be due to the restricted cation mobility in the Stern layer

660 of clays. Also, it is not sure that it is possible to correctly capture the surface conduc-
 661 tivity of clays with such linear model (de Lima & Sharma, 1990).

662 We used σ' values at 1.46 Hz for the four highest salinities (10^{-3} -1 M of NaCl) to ad-
 663 just one formation factor and one surface conductivity per clay type using equation 2.
 664 Then, we recalculated σ'_{surf} values for each salinity (using equation 3) and considered
 665 equation 4 to associate the measured values of σ'' to σ''_{surf} . Figure 9b shows the rela-
 666 tion between σ'_{surf} and σ'' . We obtained the best fit for equation 5 for $l = 0.0039$, that
 667 is, almost an order of magnitude smaller than the value of Weller et al. (2013) ($l = 0.042$)
 668 from samples containing no clay. Our data agree more with the value of l proposed by
 669 Lévy et al. (2019b) ($l = 0.002$, when samples had more than 20% smectite), than the
 670 one of Weller et al. (2013). As we only consider clay samples, this difference could be
 671 attributed to the difference in mineralogical composition. Perhaps sandstones and sed-
 672 iments behave more like what Weller et al. (2013) present, but as clay materials have a
 673 significant σ'_{surf} , they present a different, but also seemingly linear behavior.

674 In order to test the hypothesis that l decreases with clay content, in Figure 9a we eval-
 675 uated the combined dataset of Woodruff et al. (2014), Lévy et al. (2019b), and ours. For
 676 Lévy et al. (2019b) we subtracted the data that contained more than 20% smectite, from
 677 their Table 1. As mentioned previously, using only our dataset we obtain $l = 0.0039$.
 678 From Figure 9a we can see that none of the proposed values for l fit perfectly this com-
 679 bined dataset. The results are in agreement with Lévy et al. (2019b) on the idea that
 680 l seems to decrease with increasing smectite content. Further than that, these data would
 681 seem to suggest that the relation between σ'' and σ'_{surf} is a non-linear one over multi-
 682 ple types of minerals. A more thorough analysis over multiple types of minerals needs
 683 to be performed in order to determine if there is a larger obtainable linear or non-linear
 684 relation between σ'' and σ'_{surf} . Another interesting relationship that is studied between
 685 two SIP parameters is the relationship between σ'' and the surface area per unit volume
 686 (S_{por}), see Weller et al. (2015a) and Revil (2012). In the supplementary information, we
 687 present a comparison of our data and that presented in Weller et al. (2015a) and Börner
 688 (1992). It should be noted that we use clay samples and not a mix of sand and clay, and
 689 thus the results between the data presented in Weller et al. (2015a), Börner (1992), and
 690 our data do not align perfectly.

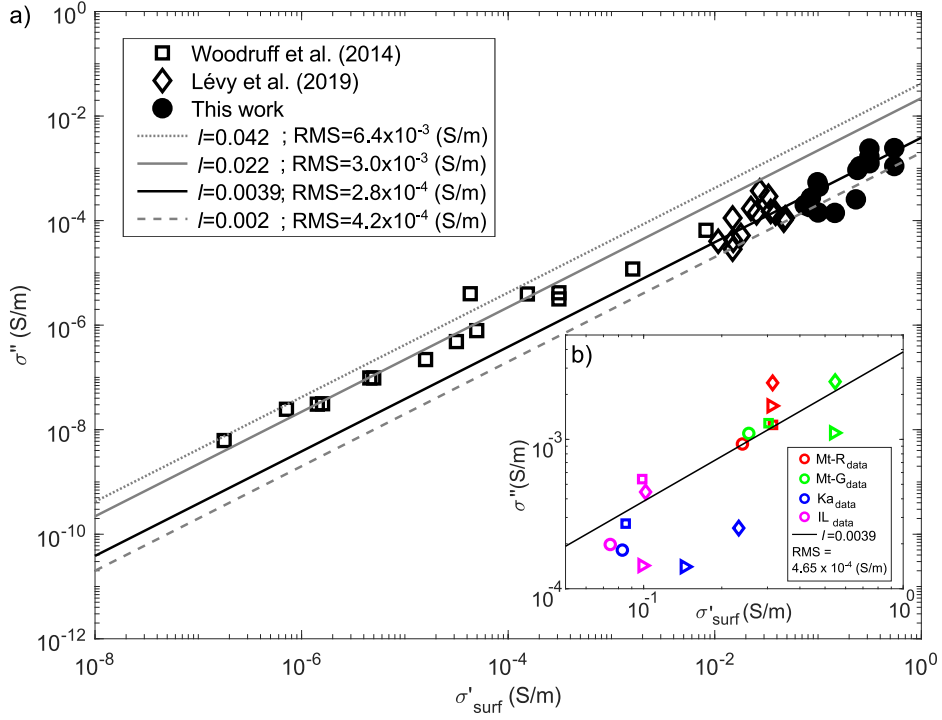


Figure 9. Relationship between σ'' and σ'_{surf} . a) Comparison of different linear parameters presented in the literature, and the datasets from Woodruff et al. (2014) and Lévy et al. (2019b). b) Linear fit ($l = 0.0039$) between σ'' and σ'_{surf} , with our data at 1.46 Hz and with the four highest salinities. The red symbols represent the red montmorillonite sample, the green represent the green montmorillonite sample, the blue symbols the kaolinite sample, and the magenta represent the illite sample. The symbols (in b) representing data from the lower to higher salinity are: circle, square, diamond, and triangle.

691 Among the various existing phenomenological models, we used a double-Pelton model
 692 to fit our data. We noticed that a double-Warburg model ($c=0.5$) was suitable for three
 693 of our datasets (kaolinite, red, and green montmorillonite samples). Revil et al. (2014)
 694 have proposed rather the use of a Warburg model over a Debye or Pelton model, after
 695 analyzing SIP datasets of metal-free and clayey materials. This holds true for three of
 696 the measured types of clay, that is the kaolinite, red and green montmorillonite samples.
 697 Only the illite sample cannot be fitted by a double-Warburg and presents the most no-
 698 ticeable mid-frequency (around 10 Hz) peak of all the measured types of clay. We present
 699 in Figure 10, trends we found among all double-Pelton parameters. To further interpret
 700 the results of the double-Pelton model, one can consider the classic formula of charge-
 701 ability (m):

$$m = \frac{\sigma_{\infty} - \sigma_0}{\sigma_{\infty}}, \quad (10)$$

702 where, σ_{∞} can be thought of as the conductivity at high frequency or the AC conduc-
 703 tivity due to polarization plus the DC conductivity, and σ_0 can be thought of as the con-
 704 ductivity at low frequency or only the DC conductivity. In this way, if we notice an in-
 705 crease of m_1 or m_2 , we could interpret this as that possibly AC conductivity increases
 706 or increases faster with respect to DC conductivity. Similarly, if we notice a decrease of
 707 m_1 or m_2 , we could interpret this as DC conductivity increasing faster than the AC con-
 708 ductivity. We see an overall decrease of m_1 with an increase of σ_0 , and we observe a de-
 709 crease of τ_2 with an increase of m_2 . We could interpret the first as a direct result of our
 710 data processing protocol. By optimizing the Pelton parameters from the curves of am-
 711 plitude and phase, we see an overall decrease of the mid-frequency peak (red peak in Fig-
 712 ure 8b) with an increase in salinity of the clay sample. We attribute the decrease of m_1
 713 with salinity to maybe the cease of a polarization mechanism at a particular salinity. The
 714 fact that we don't necessarily see a decrease of m_2 with salinity means that perhaps, at
 715 a certain salinity some other polarization mechanisms are still active. Which polariza-
 716 tion mechanism acts at which salinity is still an open question. Further investigation needs
 717 to be done, specifically on the modeling side, to better understand the SIP response of
 718 clay samples for varying salinities, with individual polarization mechanisms in mind. The
 719 correlation of τ_2 and m_2 could be an artifact present in our optimization process. How-
 720 ever, we do not see such a behavior between τ_1 and m_1 . Schwartz & Furman (2015) ad-

721 just a single Pelton on their SIP data on soil organic matter, and they also see a decrease
722 of τ with an increase of m . They attribute this phenomenon to the fact that an ion mo-
723 bility reduction causes an increase in the relaxation time and a decrease in polarization.
724 Indeed, as presented in Table 4 and Figure 10b, we see that for m_2 and τ_2 of our dataset
725 this holds truth as well. An explanation of the observed inverse correlation between m_2
726 and τ_2 could be also due to the EDL polarization of the smallest clay particles at high
727 frequency. Large clay particles tend to polarize less than smaller clay particles due to
728 their lower total specific surface area, and thus lower surface conductivity. However, the
729 relaxation time of the EDL polarization increases when the size of the particle increases.
730 Therefore, the chargeability due to these small clay particles may decrease when the re-
731 laxation time increases. More modeling work is necessary on the polarization of the EDL
732 of clay particles to better interpret our results with respect to individual polarization mech-
733 anisms, in particular the EDL polarization.

734 Our $\Delta\sigma_N^*$ calculations agree with the fact that the highest conduction and polarization
735 values come from the smectite samples. We could interpret this as a result of the fact
736 that the smectite samples have a higher specific surface area than illite sample, which
737 has a higher specific surface area than the kaolinite sample. The surface charge of mont-
738 morillonite and illite may also be higher in magnitude than the surface charge of kaoli-
739 nite. The imaginary conductivity amplitude is roughly one order of magnitude higher
740 for the montmorillonite samples than for other clay samples. Due to their higher spe-
741 cific surface area and stronger EDL, the montmorillonite samples may polarize more than
742 the kaolinite and illite samples, and this may also explain why more salt is necessary to
743 "saturate" the EDL polarization controlling imaginary conductivity. For the red and green
744 montmorillonite samples, we interpret the fact that the peak of polarization (see Figure
745 4) happens around a 10^{-1} M NaCl salinity due to the high electrical charge (see the CEC
746 values in Table 3) on the basal surfaces of all smectites. Diffuse layers around montmo-
747 rillonite particles are strongly repulsive, meaning that a high ion concentration in the
748 pore water is necessary to compress the diffuse layers which decreases membrane polar-
749 ization effects and favour coagulation of the particles (Tombácz & Szekeres, 2006). Co-
750 agulated particles exhibit a smaller external surface area available for polarization. Il-
751 lite and kaolinite have a smaller specific surface area, therefore, the peak in their imag-
752 inary conductivity may happen at a smaller ion concentration in the pore water.

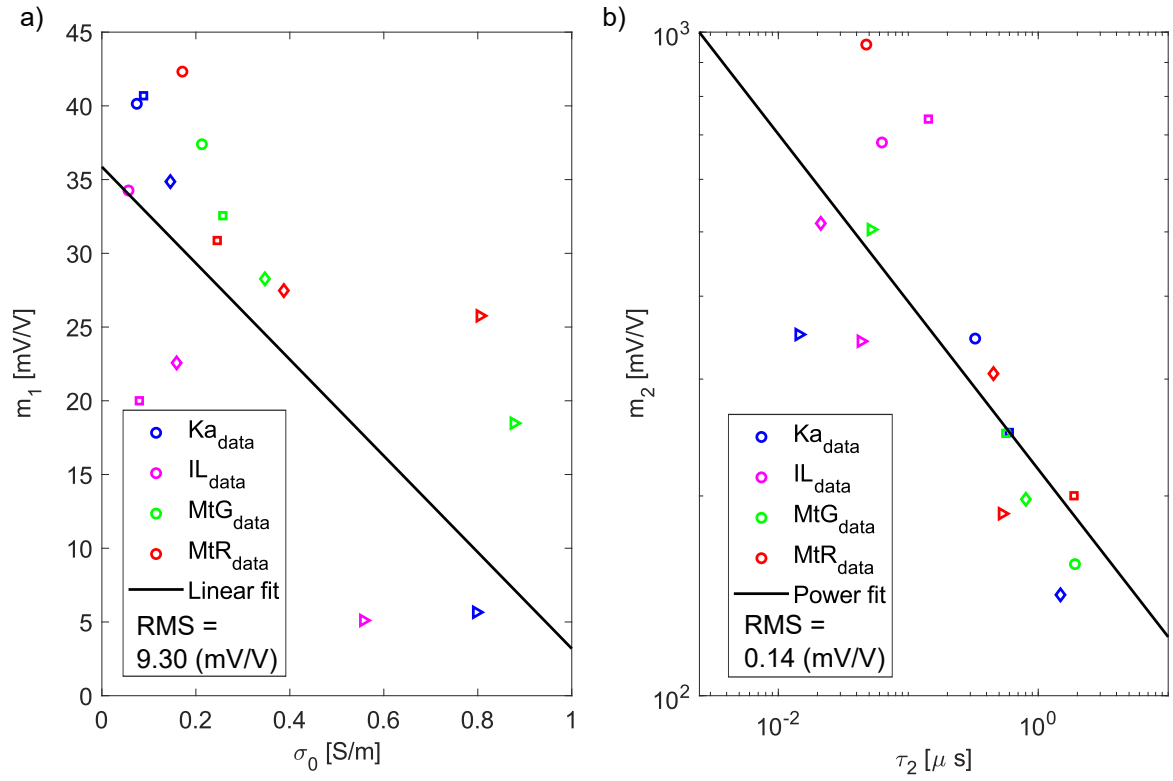


Figure 10. From the double-Pelton optimization parameters: a) dependence of m_1 and σ_0 , and b) dependence of τ_2 and m_2 . The red symbols represent the red montmorillonite sample, the green represent green montmorillonite sample, the blue the kaolinite sample, and the magenta represent the illite sample. The symbols representing data from lower to higher salinity are: circle, square, diamond, and triangle.

753 If we take a look at Figures 6 and 7, we see that for both conductivities (real and imag-
754 inary), the montmorillonite samples are less dispersed than the kaolinite and illite sam-
755 ples. Meaning, the maximum and minimum values are closer together for the montmo-
756 rillonite samples than for the illite and kaolinite samples. This could be due to the fact
757 that montmorillonites have a far more important specific surface area than illite and kaoli-
758 nite, therefore a change in salinity effects more the conductivities (real and imaginary)
759 of kaolinite and illite. Furthermore, we can observe in Figure 6 that the surface conduc-
760 tivity of the montmorillonite samples is higher than the surface conductivity of the kaoli-
761 nite and illite samples. We can see this as in the lowest salinity, we have higher values
762 for the real conductivity of the montmorillonite samples in comparison to the kaolinite
763 and illite samples. At the lowest salinity, we can assume that the surface conductivity
764 is the most important between pore water conductivity and surface conductivity (see equa-
765 tion 2). The high surface conductivity of the montmorillonite samples could also explain
766 the fact that the difference between maximum and minimum conductivities is bigger for
767 the kaolinite and illite samples, than for the montmorillonite samples (see Figure 6). Again,
768 as the salinity increases (more available ions), it can significantly effect the pore water
769 conductivity and thus the total measured conductivity of the kaolinite and illite sam-
770 ples. As for the montmorillonite samples, this is less clear because of the high surface
771 conductivity. For the montmorillonites and kaolinite samples, the imaginary conductiv-
772 ity spectra are less sensitive to salinity than for the illite sample. This may be due to
773 the permanent negative surface charge of the basal surface of montmorillonite (see Fig-
774 ure 1) which may control polarization of montmorillonites and kaolinite (to a lesser ex-
775 tent due to a significant content of smectite). In addition, the illite sample exhibits a po-
776 larization peak at a frequency of around 10 Hz, which is not seen for the other clay types
777 (flatter signals). Following Schwarz (1962), we could attribute this 10 Hz peak of polar-
778 ization in the illite sample to a possible presence of bigger clay aggregates compared to
779 the rest of the clay samples. The illite sample used for our measurements (see Table 1)
780 has 12% calcite that could perhaps correspond to polarization around big non-polarizing
781 grains.

782 In Figure 11 we present a conceptual sketch of what we interpret occurs to clay parti-
783 cles with increasing salinity. As the salinity increases, it seems plausible that clay parti-
784 cles coagulate; and thus the distance between clay particles decreases with increasing
785 salinity, up until a point of coagulation where two clay particles can be thought of as a

786 thicker clay particle. As a result, initially at the lowest salinity (Figure 11a), we have
787 two clay particles with a negative surface charge, and an overlapping diffuse layer, with
788 a membrane effect polarization. At the mid-salinity (Figure 11b), we still see an over-
789 lap in the diffuse layer, with a possible reduced membrane effect polarization. Ideally,
790 we have more salinity (NaCl), thus more available ions to polarize, and thus we see an
791 increase in polarization from Figure 11a to Figure 11b. On the contrary, at the highest
792 salinity (Figure 11c), where clay particles have coagulated and thus we have a smaller
793 external specific surface charge; a smaller area for ions to polarize. In addition, we have
794 a null membrane polarization effect at the highest salinity. To make the link with Fig-
795 ure 4b, for the montmorillonite samples, the two lowest salinities (10^{-2} - 10^{-1} S/m range)
796 would correspond to the state presented in Figure 11a, the 10^0 S/m salinity would cor-
797 respond to in Figure 11b, and the 10^1 S/m would correspond to Figure 11c. For the kaoli-
798 nite and illite samples, we would rather couple the 10^{-2} S/m (presented in Figure 4b)
799 to Figure 11a, the 10^{-1} S/m to Figure 11b, and finally the two highest salinities (10^0 -
800 10^1 S/m range) to 11c. This is consistent with, Vinegar & Waxman (1984), who proposed
801 that the decrease of the quadrature conductivity with salinity in shaly sands happens
802 due to a decrease of the membrane effect. Revil (2012) mentions that there is a relative
803 change on the effect of polarization mechanisms with salinity. Furthermore, Hördt et al.
804 (2016) made a numerical membrane polarization study of wide and narrow pores of dif-
805 ferent sizes and varying salinity and pH. They find that specially for narrow pores, the
806 imaginary conductivity increases with salinity until a maximum value, and then decreases.
807 Additionally, Weller et al. (2015b) and Lesmes & Frye (2001) have interpreted the de-
808 crease of the polarization at a high salinity by a decrease of the ionic mobility at high
809 salinities. Although according to molecular dynamics (MD) predictions (Bourg & Spos-
810 ito, 2011), the mobility of counter-ions (Na^+) in the Stern layer does not decrease when
811 salinity increases. More physical or numerical modeling of clays needs to be done to bet-
812 ter understand exactly how each phenomenon (clay coagulation and decrease of ionic mo-
813 bility) effects the polarization of clay samples at varying salinities.

814 On the differentiation of clay types by using SIP, we can think of two things. If we take
815 a look at the parameters of Table 4, we could say these parameters are very close to each
816 other, and on a field scale experiment, realistically differentiating two types of clay seems
817 very ambitious. The success of such a task would depend on the fieldwork planning, so
818 a correct resolution is used, but with single parameters such as σ_0 , the task would seem

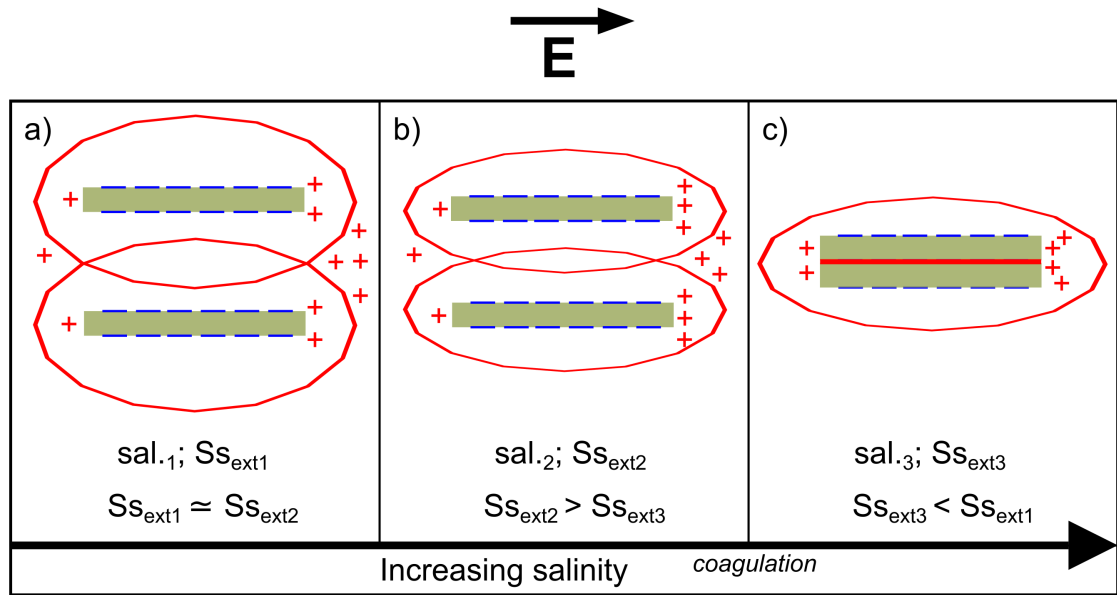


Figure 11. An interpreted process of how clay particles behave with increasing salinity. The state of two clay particles at a) the lowest salinity, b) mid-salinity and c) highest salinity. In green we present individual clay particles. In blue the negative surface charge of the clay particle, and in red the EDL (Stern and diffuse layer). In this figure, we refer to *sal.* to salinity, and Ss_{ext} to the specific surface area of the clay particle. Numbers 1, 2, and 3 represent different stages of increasing salinity and therefore coagulation.

819 complicated. However, if we take a look at figures 6 and 7, differentiating types of clay
820 using multiple frequencies seems easier of a task. Therefore, if a fieldwork campaign is
821 carried out with the objective of differentiating two or more types of clay in a formation,
822 we recommend using multi-frequency electrical methods. Moreover, differentiating two
823 types of montmorillonites in the field and laboratory scale seems impossible if only us-
824 ing geo-electrical methods. However, differentiating between a montmorillonite and il-
825 lite or kaolinite seems more achievable of a task in both the field and laboratory scales.
826 Knowing that in the laboratory we have a controlled experiment, using relatively pure
827 clay and that in the field, we don't have a controlled system in a more complex (hetero-
828 geneous) system.

829 Zonge et al. (2005) mention that the differentiation of clay types in IP is possible at fre-
830 quencies above 1000 Hz. Our dataset could help establishing a basis to differentiate types
831 of clay at lower frequencies (<1000 Hz) using the widely used low frequency geo-electrical
832 methods. We understand that, just because we can see a clear difference in the resistiv-
833 ity values of our clay samples (see Table 5), this does not necessarily mean that, this dif-
834 ferentiation could be done for all field conditions. Differentiating types of clay would de-
835 pend on the clay samples themselves and the resolution of method used for the data col-
836 lection in the field. As future work, we could use our dataset as a basis for forward-modeling
837 to better understand if the differentiation of types of clay would be possible at the field
838 scale. Also more experiments at a larger laboratory scale (pluri-decimetric) to test if we
839 are able to differentiate types of clay using geo-electrical methods in a controlled envi-
840 ronment.

841 **6 Conclusions**

842 We present a new laboratory protocol to characterize clay samples with good re-
843 peatability, and a new SIP dataset consisting of four different types of clay (red and green
844 montmorillonite samples, an illite sample, and a kaolinite sample) at five different NaCl
845 salinities (from initially de-ionized water to 1 M NaCl). Our data shows an increase of
846 the real part of the conductivity with salinity, while there is a non-monotonous behav-
847 ior with the imaginary conductivity. A possible interpretation of this behavior could be
848 that as salinity increases, coagulation happens. At a particular salinity threshold some
849 polarization mechanisms cease to act, possibly membrane polarization effects, thus de-
850 creasing at a particular salinity the imaginary conductivity of the clay sample. There

851 is a difference in the peak of polarization between clay types, varying both with salin-
852 ity and in amplitude. Montmorillonite samples may present this polarizability peak at
853 a higher salinity than the kaolinite and illite samples. This agrees with the fact that smec-
854 tites need a higher ion concentration in the pore water to diminish membrane polariza-
855 tion effects and favour particles coagulation. We calculate the surface conductivities of
856 the clay samples for the four highest salinities and we confirm that both montmorillonite
857 samples have higher surface conductivities with respect to the kaolinite and illite sam-
858 ples and correlate well with the measured CEC. We found the linear parameter (l) be-
859 tween both surface conductivities to be 0.0039 for our dataset. A wider dataset of clayey
860 materials would seem to suggest that l decreases with clay content.

861 More work on the side of the physical modeling needs to be done in order to be able to
862 interpret our dataset by polarization mechanisms. Additionally more laboratory work,
863 at a slightly bigger scale (pluri-decimetric) or directly field scale using multi-frequency
864 geo-electrical methods could be used to validate the differentiation of clay types at big-
865 ger scales.

866 **Acknowledgments**

867 The authors strongly thank the financial support of ANR EXCITING (grant ANR-17-
868 CE06-0012) for this work and for the PhD thesis funding of A. Mendieta. We would also
869 like to thank: Claude Fontaine, Philippe Cosenza, Céline Boissard, and Patricia Patrier.
870 Members of the HydrASA team of the University of Poitiers for performing the XRD
871 and CEC measurements on the different types of clay samples. The data used in this study
872 will be available at the doi:10.5281/zenodo.4050345 after acceptance of the paper.

873 **References**

- 874 Auken, E., Boesen, T., & Christiansen, A. V. (2017). A Review of Airborne Elec-
875 tromagnetic Methods With Focus on Geotechnical and Hydrological Applications
876 From 2007 to 2017. In *Advances in geophysics* (Vol. 58, pp. 47–93). Elsevier Inc.
877 doi: 10.1016/bs.agph.2017.10.002
- 878 Batayneh, A. T. (2006). Resistivity tomography as an aid to planning gas-pipeline
879 construction, Risha area, north-east Jordan. *Near Surface Geophysics*, *4*, 313–319.
880 doi: 10.3997/1873-0604.2005053
- 881 Bergaya, F., & Lagaly, G. (2006). General introduction: clays, clay minerals, and

- 882 clay science. In B. F., T. B.K.G., & L. G. (Eds.), *Handbook of clay science* (1st
883 ed., Vol. 1, pp. 1–18). Elsevier Ltd. doi: 10.1016/S1572-4352(05)01001-9
- 884 Börner, F. (1992). Complex conductivity measurements of reservoir properties.
885 In P. Worthington & C. Chardaire-Rivière (Eds.), *Advances in core evaluation:
886 Reservoir management: Reviewed proceedings of the society for core analysis third
887 european core analysis symposium* (pp. 359–386). Hardwood Academic.
- 888 Bourg, I. C., & Sposito, G. (2011). Molecular dynamics simulations of the electri-
889 cal double layer on smectite surfaces contacting concentrated mixed electrolyte
890 (NaCl-CaCl₂) solutions. *Journal of Colloid And Interface Science*, *360*(2), 701–
891 715. Retrieved from <http://dx.doi.org/10.1016/j.jcis.2011.04.063> doi:
892 10.1016/j.jcis.2011.04.063
- 893 Breede, K., Kemna, A., Esser, O., Zimmermann, E., Vereecken, H., & Huisman,
894 J. A. (2012). Spectral induced polarization measurements on variably sat-
895 urated sand-clay mixtures. *Near Surface Geophysics*, *10*, 479–489. doi:
896 10.3997/1873-0604.2012048
- 897 Brigatti, M. F., Galan, E., & Theng, B. K. (2006). Structures and Mineralogy of
898 Clay Minerals. In B. F., T. B.K.G., & L. G. (Eds.), *Handbook of clay science*
899 (Vol. 1, pp. 19–86). Elsevier Ltd. doi: 10.1016/S1572-4352(05)01002-0
- 900 Brindley, G., & Brown, G. (1980). *Crystal structures of Clay Minerals and Their
901 X-ray Identification. Mineralogical Society Monograph No. 5*. London: The Miner-
902 alogical Society of Great Britain and Ireland.
- 903 Bückner, M., Flores Orozco, A., Undorf, S., & Kemna, A. (2019). On the Role of
904 Stern- and Diffuse-Layer Polarization Mechanisms in Porous Media. *Journal of
905 Geophysical Research: Solid Earth*, *124*, 5656–5677. doi: 10.1029/2019JB017679
- 906 Bückner, M., & Hördt, A. (2013). Analytical modelling of membrane polarization
907 with explicit parametrization of pore radii and the electrical double layer. *Geo-
908 physical Journal International*, *194*, 804–813. doi: 10.1093/gji/ggt136
- 909 Caceci, M., & Cacheris, W. (1984). Fitting curves to data. The Simplex algorithm is
910 the answer. *Byte*, *9*, 340–362.
- 911 Chen, Y., & Or, D. (2006). Effects of Maxwell-Wagner polarization on soil complex
912 dielectric permittivity under variable temperature and electrical conductivity. *Wa-
913 ter Resources Research*, *42*, 1–14. doi: 10.1029/2005WR004590
- 914 Chorover, J., Kretschmar, R., Garica-Pichel, F., & Sparks, D. L. (2007). Soil bio-

- 915 geochemical processes within the critical zone. *Elements*, *3*, 321–326. doi: 10
916 .2113/gselements.3.5.321
- 917 Chung, F. H. (1974). Quantitative interpretation of X-ray diffraction patterns of
918 mixtures. I. Matrix-flushing method for quantitative multicomponent analysis.
919 *Journal of Applied Crystallography*, *7*, 519–525. doi: 10.1107/s0021889874010375
- 920 Ciesielski, H., & Sterckeman, T. (1997). Determination of cation exchange capacity
921 and exchangeable cations in soils by means of cobalt hexamine trichloride. Effects
922 of experimental conditions. *Agronomie*, *17*, 1–7. doi: 10.1051/agro:19970101
- 923 Cole, K. S., & Cole, R. H. (1941). Dispersion and Absorption in Dielectrics. *Journal*
924 *of Chemical Physics*, *9*, 341. doi: <https://doi.org/10.1063/1.1750906>
- 925 Corrado, S., Aldega, L., Celano, A. S., De Benedetti, A. A., & Giordano, G. (2014).
926 Cap rock efficiency and fluid circulation of natural hydrothermal systems by
927 means of XRD on clay minerals (Sutri, Northern Latium, Italy). *Geothermics*, *50*,
928 180–188. doi: 10.1016/j.geothermics.2013.09.011
- 929 Cosenza, P., Ghorbani, A., Revil, A., Zamora, M., Schmutz, M., Jougnot, D.,
930 & Florsch, N. (2008). A physical model of the low-frequency electrical po-
931 larization of clay rocks. *Journal of Geophysical Research*, *113*, 1–9. doi:
932 10.1029/2007JB005539
- 933 de Lima, O. A., & Sharma, M. M. (1990). A grain conductivity approach to
934 shaly sandstones. *Geophysics*, *55*, 1347–1356. doi: [doi:https://doi.org/10.1190/](https://doi.org/10.1190/1.1442782)
935 [1.1442782](https://doi.org/10.1190/1.1442782)
- 936 Finco, C., Pontoreau, C., Schamper, C., Massuel, S., Hovhannissian, G., & Rejiba,
937 F. (2018). Time-domain electromagnetic imaging of a clayey confining bed in a
938 brackish environment: A case study in the Kairouan Plain Aquifer (Kelbia salt
939 lake, Tunisia). *Hydrological Processes*, *32*, 3954–3965. doi: 10.1002/hyp.13303
- 940 Garrels, R. M., & Mackenzie, F. (1971). *Evolution of sedimentary rocks*. New York.
- 941 Ghorbani, A., Cosenza, P., Revil, A., Zamora, M., Schmutz, M., Florsch, N., &
942 Jougnot, D. (2009). Non-invasive monitoring of water content and textural
943 changes in clay-rocks using spectral induced polarization: A laboratory investiga-
944 tion. *Applied Clay Science*, *43*, 493–502. doi: 10.1016/j.clay.2008.12.007
- 945 Gonçalves, J., de Marsily, G., & Tremosa, J. (2012). Importance of thermo-
946 osmosis for fluid flow and transport in clay formations hosting a nuclear
947 waste repository. *Earth and Planetary Science Letters*, *339-340*, 1–10. doi:

- 948 10.1016/j.epsl.2012.03.032
- 949 Hassan, M. S., Villieras, F., Gaboriaud, F., & Razafitianamaharavo, A. (2006).
 950 AFM and low-pressure argon adsorption analysis of geometrical properties of
 951 phyllosilicates. *Journal of Colloid and Interface Science*, *296*, 614–623. doi:
 952 10.1016/j.jcis.2005.09.028
- 953 Hillier, S. (2003). Quantitative Analysis of Clay and other Minerals in Sandstones by
 954 X-Ray Powder Diffraction (XRPD). *Int. Assoc. Sedimentol. Spec. Publ.*, *34*, 213–
 955 251. doi: 10.1002/9781444304336.ch11
- 956 Hördt, A., Bairlein, K., Bielefeld, A., Bücken, M., Kuhn, E., Nordsiek, S., & Stebner,
 957 H. (2016). The dependence of induced polarization on fluid salinity and pH,
 958 studied with an extended model of membrane polarization. *Journal of Applied
 959 Geophysics*, *135*, 408–417. doi: 10.1016/j.jappgeo.2016.02.007
- 960 Huisman, J. A., Zimmermann, E., Esser, O., Haegel, F. H., Treichel, A., &
 961 Vereecken, H. (2016). Evaluation of a novel correction procedure to remove elec-
 962 trode impedance effects from broadband SIP measurements. *Journal of Applied
 963 Geophysics*, *135*, 466–473. doi: 10.1016/j.jappgeo.2015.11.008
- 964 Islam, M., Chittoori, B., & Burbank, M. (2020). Evaluating the Applicability of
 965 Biostimulated Calcium Carbonate Precipitation to Stabilize Clayey Soils. *Journal
 966 of Materials in Civil Engineering*, *32*, 1–11. doi: 10.1061/(ASCE)MT.1943-5533
 967 .0003036
- 968 Jougnot, D., Ghorbani, A., Revil, A., Leroy, P., & Cosenza, P. (2010). Spectral in-
 969 duced polarization of partially saturated clay-rocks : a mechanistic approach. *Geo-
 970 physical Journal International*, *180*, 210–224. doi: 10.1111/j.1365-246X.2009.04426
 971 .x
- 972 Kemna, A., Binley, A., Cassiani, G., Niederleithinger, E., Revil, A., Slater, L., ...
 973 Zimmermann, E. (2012). An overview of the spectral induced polarization
 974 method for near-surface applications. *Near Surface Geophysics*, *10*, 453–468.
 975 doi: 10.3997/1873-0604.2012027
- 976 Khaled, E. M., & Stucki, J. W. (1991). Iron Oxidation State Effects on Cation Fixa-
 977 tion in Smectites. *Soil Science Society of America Journal*, *55*(2), 550–554.
- 978 Konikow, L., August, L., & Voss, C. (2001). Effects of clay dispersion on aquifer
 979 storage and recovery in coastal aquifers. *Transport in Porous Media*, *43*, 45–64.
 980 doi: 10.1023/A:1010613525547

- 981 Kremer, T., Schmutz, M., Maineult, A., & Agrinier, P. (2016). Laboratory mon-
982 itoring of CO₂ injection in saturated silica and carbonate sands using spectral
983 induced polarization. *Geophysical Journal International*, *207*, 1258–1272. doi:
984 10.1093/gji/ggw333
- 985 Leroy, P., & Revil, A. (2004). A triple-layer model of the surface electrochemical
986 properties of clay minerals. *Journal of Colloid and Interface Science*, *270*, 371–
987 380. doi: 10.1016/j.jcis.2003.08.007
- 988 Leroy, P., & Revil, A. (2009). A mechanistic model for the spectral induced polariza-
989 tion of clay materials. *Journal of Geophysical Research*, *114*(B10202), 1–21. doi:
990 10.1029/2008JB006114
- 991 Leroy, P., Tournassat, C., Bernard, O., Devau, N., & Azaroual, M. (2015). The
992 electrophoretic mobility of montmorillonite. Zeta potential and surface con-
993 ductivity effects. *Journal of Colloid And Interface Science*, *451*, 21–39. doi:
994 10.1016/j.jcis.2015.03.047
- 995 Leroy, P., Weigand, M., Mériquet, G., Zimmermann, E., Tournassat, C., Fager-
996 lund, F., . . . Huisman, J. A. (2017). Spectral induced polarization of Na-
997 montmorillonite dispersions. *Journal of Colloid And Interface Science*, *505*,
998 1093–1110. doi: 10.1016/j.jcis.2017.06.071
- 999 Lesmes, D. P., & Frye, K. M. (2001). Influence of pore fluid chemistry on the com-
1000 plex conductivity and induced polarization responses of Berea sandstone. *Journal*
1001 *of Geophysical Research: Solid Earth*(B3), 4079–4090. doi: 10.1029/2000jb900392
- 1002 Lévy, L., Gibert, B., Sigmundsson, F., Flóvenz, O. G., Hersir, G. P., Briole, P., &
1003 Pezard, P. A. (2018). The role of smectites in the electrical conductivity of
1004 active hydrothermal systems: Electrical properties of core samples from Krafla
1005 volcano, Iceland. *Geophysical Journal International*, *215*, 1558–1582. doi:
1006 10.1093/gji/ggy342
- 1007 Lévy, L., Maurya, P. K., Byrdina, S., Vandemeulebrouck, J., Sigmundsson, F.,
1008 Árnason, K., . . . Labazuy, P. (2019a). Electrical resistivity tomography and
1009 time-domain induced polarization field investigations of geothermal areas at
1010 Krafla, Iceland: Comparison to borehole and laboratory frequency-domain elec-
1011 trical observations. *Geophysical Journal International*, *218*, 1469–1489. doi:
1012 10.1093/gji/ggz240
- 1013 Lévy, L., Weller, A., & Gibert, B. (2019b). Influence of smectite and salinity on the

- 1014 imaginary and surface conductivity of volcanic rocks. *Near Surface Geophysics*,
 1015 *17*, 653–673. doi: 10.1002/nsg.12069
- 1016 Looms, M. C., Klotzsche, A., van der Kruk, J., Larsen, T. H., Edsen, A., Tuxen, N.,
 1017 ... Nielsen, L. (2018). Mapping sand layers in clayey till using crosshole ground-
 1018 penetrating radar. *Geophysics*, *83*, A21–A26. doi: 10.1190/GEO2017-0297.1
- 1019 Ma, C., & Eggleton, R. (1999). Cation Exchange Capacity of Kaolinite. *Clays and*
 1020 *Clay Minerals*, *47*, 174–180. doi: <https://doi.org/10.1346/CCMN.1999.0470207>
- 1021 Maineult, A. (2016). Estimation of the electrical potential distribution along metal-
 1022 lic casing from surface self-potential profile. *Journal of Applied Geophysics*, *129*,
 1023 66–78. doi: 10.1016/j.jappgeo.2016.03.038
- 1024 Maineult, A., Revil, A., Camerlynck, C., Florsch, N., & Titov, K. (2017). Upscaling
 1025 of spectral induced polarization response using random tube networks. *Geophysi-
 1026 cal Journal International*, *209*, 948–960. doi: 10.1093/gji/ggx066
- 1027 Meier, L. P., & Kahr, G. (1999). Determination of the Cation Exchange Capac-
 1028 ity (CEC) of Clay Minerals Using the Complexes of Copper(II) Ion with Tri-
 1029 ethylenetetramine and Tetraethylenepentamine. *Clays and Clay Minerals*, *47*(3),
 1030 386–388. doi: 10.1346/ccmn.1999.0470315
- 1031 Michot, L. J., & Villieras, F. (2006). Surface Area and Porosity. In F. Bergaya,
 1032 B. K. Theng, & G. Lagaly (Eds.), *Handbook of clay science* (Vol. 1, pp. 965–978).
 1033 Elsevier Ltd. doi: 10.1016/S1572-4352(05)01035-4
- 1034 Mitchell, J. K., & Soga, K. (2005). *Fundamentals of Soil Behavior* (3rd ed.). John
 1035 Wiley & Sons. doi: 10.1097/00010694-199407000-00009
- 1036 Moore, D., & Reynolds, R. (1989). *X-ray diffraction and the identification and anal-
 1037 ysis of clay minerals*. Oxford University Press.
- 1038 Morsy, S., & Sheng, J. (2014). Effect of Water Salinity on Shale Reservoir Produc-
 1039 tivity. *Advances in Petroleum Exploration and Development*, *8*, 9–14. doi: 10
 1040 .3968/5604
- 1041 Okay, G., Cosenza, P., Ghorbani, A., Camerlynck, C., Cabrera, J., Florsch, N., &
 1042 Revil, A. (2013). Localization and characterization of cracks in clay-rocks using
 1043 frequency and time-domain induced polarization. *Geophysical Prospecting*, *61*,
 1044 134–152. doi: 10.1111/j.1365-2478.2012.01054.x
- 1045 Okay, G., Leroy, P., Ghorbani, A., Cosenza, P., Camerlynck, C., Cabrera, J., ... Re-
 1046 vil, A. (2014). Spectral induced polarization of clay-sand mixtures : Experiments

- 1047 and modeling. *Geophysics*, *79*, 353–375. doi: 10.1190/GEO2013-0347.1
- 1048 Ortiz, L., Volckaert, G., & Mallants, D. (2002). Gas generation and migration in
1049 Boom Clay, a potential host rock formation for nuclear waste storage. *Engineering*
1050 *Geology*, *64*, 287–296. doi: 10.1016/S0013-7952(01)00107-7
- 1051 Parker, B. L., Chapman, S. W., & Guilbeault, M. A. (2008). Plume persistence
1052 caused by back diffusion from thin clay layers in a sand aquifer following TCE
1053 source-zone hydraulic isolation. *Journal of Contaminant Hydrology*, *102*, 86–104.
1054 doi: 10.1016/j.jconhyd.2008.07.003
- 1055 Pelton, W., Ward, S. H., Hallof, P. G., Sill, W. R., & Nelson, P. H. (1978). Mineral
1056 discrimination and removal of inductive coupling with multifrequency IP. *Geophy-*
1057 *ics*, *43*, 588–609. doi: <https://doi.org/10.1190/1.1440839>
- 1058 Revil, A. (2012). Spectral induced polarization of shaly sands: Influence of the
1059 electrical double layer. *Water Resources Research*, *48*(2), 1–23. doi: 10.1029/
1060 2011WR011260
- 1061 Revil, A., Florsch, N., & Camerlynck, C. (2014). Spectral induced polarization
1062 porosimetry. *Geophysical Journal International*, *198*, 1016–1033. doi: 10.1093/gji/
1063 ggu180
- 1064 Revil, A., Karaoulis, M., Johnson, T., & Kemna, A. (2012). Review : Some low-
1065 frequency electrical methods for subsurface characterization and monitoring in hy-
1066 drogeology. *Hydrogeology Journal*, *20*, 617–658. doi: 10.1007/s10040-011-0819-x
- 1067 Revil, A., & Leroy, P. (2004). Constitutive equations for ionic transport in porous
1068 shales. *Journal of Geophysical Research*, *109*, 1–19. doi: 10.1029/2003jb002755
- 1069 Revil, A., & Skold, M. (2011). Salinity dependence of spectral induced polarization
1070 in sands and sandstones. *Geophysical Journal International*, *187*, 813–824. doi: 10
1071 .1111/j.1365-246X.2011.05181.x
- 1072 Schwartz, N., & Furman, A. (2015). On the spectral induced polarization signature
1073 of soil organic matter. *Geophysical Journal International*, *200*, 589–595. doi: 10
1074 .1093/gji/ggu410
- 1075 Schwarz, G. (1962). A theory of the low-frequency dielectric dispersion of colloidal
1076 particles in electrolyte solution. *Journal of Physical Chemistry*, *66*, 2636–2642.
1077 doi: 10.1021/j100818a067
- 1078 Sondi, I., Biscan, J., & Pravdic, V. (1996). Electrokinetics of Pure Clay Minerals
1079 Revisited. *Journal of Colloid And Interface Science*, *178*, 514–522. doi: <https://>

- doi.org/10.1006/jcis.1996.0403
- 1080
1081 Spichak, V., & Manzella, A. (2009). Electromagnetic sounding of geothermal zones.
1082 *Journal of Applied Geophysics*, *68*, 459–478. doi: 10.1016/j.jappgeo.2008.05.007
- 1083 Tombácz, E., & Szekeres, M. (2006). Surface charge heterogeneity of kaolinite in
1084 aqueous suspension in comparison with montmorillonite. *Applied Clay Science*,
1085 *34*, 105–124. doi: 10.1016/j.clay.2006.05.009
- 1086 Tournassat, C., Bizi, M., Braibant, G., & Crouzet, C. (2011). Influence of montmo-
1087 rillonite tactoid size on Na-Ca cation exchange reactions. *Journal of Colloid and*
1088 *Interface Science*, *364*, 443–454. doi: 10.1016/j.jcis.2011.07.039
- 1089 Tournassat, C., Bourg, I. C., Steefel, C. I., & Bergaya, F. (2015). Surface Prop-
1090 erties of Clay Minerals. In C. Tournassat, C. I. Steefel, I. C. Bourg, & F. Bergaya
1091 (Eds.), *Developments in clay science* (Vol. 6, pp. 5–31). Elsevier. doi: 10.1016/
1092 B978-0-08-100027-4.00001-2
- 1093 Tournassat, C., Grangeon, S., Leroy, P., & Giffaut, E. (2013). Modeling specific pH
1094 dependent sorption of divalent metals on montmorillonite surfaces. A review of
1095 pitfalls, recent achievements and current challenges. *American Journal of Science*,
1096 *313*, 395–451.
- 1097 Tournassat, C., Neaman, A., Villéras, F., Bosbach, D., & Charlet, L. (2003).
1098 Nanomorphology of montmorillonite particles: Estimation of the clay edge sorp-
1099 tion site density by low-pressure gas adsorption and AFM observations. *American*
1100 *Mineralogist*, *88*, 1989–1995. doi: 10.2138/am-2003-11-1243
- 1101 Tournassat, C., & Steefel, C. I. (2015). Ionic transport in nano-porous clays with
1102 consideration of electrostatic effects. *Reviews in Mineralogy & Geochemistry*, *80*,
1103 287–329. doi: <http://dx.doi.org/10.2138/rmg.2015.80.09>
- 1104 Tournassat, C., & Steefel, C. I. (2019). Reactive Transport Modeling of Coupled
1105 Processes in Nanoporous Media. *Reviews in Mineralogy and Geochemistry*, *85*,
1106 75–109. doi: 10.2138/rmg.2019.85.4
- 1107 Tsujimoto, Y., Chassagne, C., & Adachi, Y. (2013). Dielectric and electrophoretic
1108 response of montmorillonite particles as function of ionic strength. *Journal of Col-*
1109 *loid and Interface Science*, *404*, 72–79. doi: 10.1016/j.jcis.2013.03.033
- 1110 Vinegar, H. J., & Waxman, M. H. (1984). Induced Polarization of Shaly Sands - the
1111 Effect of Clay Counterion Type. *Log Analyst*, *25*, 11–21.
- 1112 Wagner, J. F. (2013). Mechanical properties of clays and clay minerals. In

- 1113 F. Bergaya & G. Lagaly (Eds.), *Handbook of clay science* (2nd ed., Vol. 5A, pp.
1114 347–381). Elsevier Inc. doi: 10.1016/B978-0-08-098258-8.00011-0
- 1115 Wang, C., & Slater, L. D. (2019). Extending accurate spectral induced polarization
1116 measurements into the kHz range: Modelling and removal of errors from interac-
1117 tions between the parasitic capacitive coupling and the sample holder. *Geophysical*
1118 *Journal International*, 218, 895–912. doi: 10.1093/gji/ggz199
- 1119 Waxman, M. H., & Smits, L. J. (1968). Electrical Conductivities in Oil-Bearing
1120 Shaly Sands. *Society of Petroleum Engineers Journal*, 243, 107–122. doi: 10.2118/
1121 1863-A
- 1122 Weller, A., & Slater, L. (2012). Salinity dependence of complex conductivity of un-
1123 consolidated and consolidated materials: Comparisons with electrical double layer
1124 models. *Geophysics*, 77, D185–D198. doi: 10.1190/geo2012-0030.1
- 1125 Weller, A., Slater, L., Huisman, J. A., Esser, O., & Haegel, F. H. (2015a). On the
1126 specific polarizability of sands and sand-clay mixtures. *Geophysics*, 80, A57–A61.
1127 doi: 10.1190/GEO2014-0509.1
- 1128 Weller, A., Slater, L., & Nordsiek, S. (2013). On the relationship between in-
1129 duced polarization and surface conductivity: Implications for petrophysical
1130 interpretation of electrical measurements. *Geophysics*, 78, D315–D325. doi:
1131 10.1190/GEO2013-0076.1
- 1132 Weller, A., Slater, L., Nordsiek, S., & Ntarlagiannis, D. (2010). On the estima-
1133 tion of specific surface per unit pore volume from induced polarization: A robust
1134 empirical relation fits multiple data sets. *Geophysics*, 75, WA105–WA112. doi:
1135 10.1190/1.3471577
- 1136 Weller, A., Zhang, Z., & Slater, L. (2015b). High-salinity polarization of sandstones.
1137 *Geophysics*(3), D309–D318. doi: 10.1190/GEO2014-0483.1
- 1138 White, W. A. (1949). Atterberg plastic limits of clay minerals. *American Mineralo-*
1139 *gist*, 34, 508–512. doi: <https://doi.org/>
- 1140 Woodruff, W. F., Revil, A., & Torres-Verdín, C. (2014). Laboratory determina-
1141 tion of the complex conductivity tensor of unconventional anisotropic shales. *Geo-*
1142 *physics*, 79, E183–E200. doi: 10.1190/GEO2013-0367.1
- 1143 Zanetti, C., Weller, A., Vennetier, M., & Mériaux, P. (2011). Detection of buried
1144 tree root samples by using geoelectrical measurements: A laboratory experiment.
1145 *Plant Soil*, 339, 273–283. doi: 10.1007/s11104-010-0574-0

- 1146 Zimmermann, E., Kemna, A., Berwix, J., Glaas, W., Münch, H. M., & Huisman,
1147 J. A. (2008). A high-accuracy impedance spectrometer for measuring sediments
1148 with low polarizability. *Measurement Science and Technology*, *19*, 1–9. doi:
1149 10.1088/0957-0233/19/10/105603
- 1150 Zonge, K., Wynn, J., & Urquhart, S. (2005). Resistivity, induced polarization,
1151 and complex resistivity. In D. K. Butler (Ed.), *Near surface geophysics* (pp.
1152 265–300). Society of Exploration Geophysicists. doi: [https://doi.org/10.1190/](https://doi.org/10.1190/1.9781560801719.ch9)
1153 1.9781560801719.ch9